In situ neutron diffraction reveals the effect of Cu micro-alloying on low-temperature tensile properties of TWIP steels

Tang, Lei; Jiang, Fuqing; Liu, Huibin; Kabra, Saurabh; Cai, Biao

DOI:
10.1016/j.msea.2022.143211

Document Version
Peer reviewed version

Citation for published version (Harvard):
Tang, L, Jiang, F, Liu, H, Kabra, S & Cai, B 2022, 'In situ neutron diffraction reveals the effect of Cu micro-alloying on low-temperature tensile properties of TWIP steels', *Materials Science and Engineering A*, vol. 845, 143211. https://doi.org/10.1016/j.msea.2022.143211

In situ neutron diffraction reveals the effect of Cu micro-alloying on low-temperature tensile properties of TWIP steels

L. Tang[a], F.Q. Jiang[b], H.B. Liu[c], S. Kabra[d], B. Cai[a*]

[a] School of Metallurgy and Materials, University of Birmingham, B15 2TT, United Kingdom
[b] Institute of Metal Research, Chinese Academy of Sciences, Shenyang 110016, China
[c] Baoshan Iron & Steel CO., LTD, Shanghai 201900, China
[d] ISIS Facility, Rutherford Appleton Laboratory, Didcot OX11 0QX, United Kingdom
* Corresponding author
E-mail address: b.cai@bham.ac.uk

Abstract

High manganese steels are emerging as promising structural materials for cryogenic applications due to their low production cost and great potential in achieving excellent strength-ductility combinations. Micro-alloying serves as a desirable method in tailoring stacking fault energy (SFE) of the steels and thus tailoring the mechanical performance. In this study, we investigated the dedicate role of Cu addition played on the mechanical and microstructural responses of high manganese steels at the low-temperature range (293, 173, and 77 K) via *in situ* neutron diffraction and microscope characterizations. The addition of 1wt.%Cu to the steel not only effectively improved the yield strength (YS) and elongation but also increased the SFE thus postponing the martensite formation. For both high Mn steels, as deformation temperature decreased, the tensile strength was increased linearly, the formation of stacking faults and dislocation was promoted, and the SFE almost linearly decreased with a slope of about 0.06 $mJm^{-2}\cdot K^{-1}$. The contributions to YS and flow stress from lattice friction, grain boundary, dislocation, deformation twins, and phase transformation were determined based on neutron diffraction results and previously validated models. The work revealed the critical role of Cu addition in tailoring the SFE of TWIP steels and the resulting deformation mechanisms, paving the way in adapting new high manganese steels for cryogenic applications.

Keywords

High manganese steel, cryogenic deformation, neutron diffraction, stacking fault energy

1. Introduction

High-Mn (15-30 wt.%) steels are exhibiting ever-growing importance as structural materials in multiple cryogenic applications from liquid natural gas storage/transmission to superconducting magnets due to their excellent strength-ductility balance, desirable strength/weight ratio [1], and lower cost compared to other austenite steels [2], and 9 % Ni steels [3]. Recently, more prominent strengthening effects and excellent strength-ductility combinations of high Mn steels in a low-temperature range were reported [4–6]. The superior mechanical performance of high-Mn steels originates from their ability to synergistically activate multiple strengthening mechanisms, including dislocation motions, TWinning-Induced-Plasticity (TWIP), and TRansformation-Induced-Plasticity (TRIP) effects. The TWIP effect can be achieved by introducing dense strain-induced twin boundaries (TBs) to impede dislocation motion, while the TRIP effect can be activated when the parent austenitic face-centered cubic (FCC) austenite is transferred into martensite with hexagonal close-packed (HCP)/body-centered tetragonal (BCT) structure under strain [7]. The dominant deformation mechanism of the high-Mn steels is strongly dependent on their inherent stacking fault energy (SFE) [8–10], which is defined as the excess energy required to dissociate perfect dislocations and separate partial dislocations infinitely. The decrease of SFE can lead to the shifting of the dominant deformation mechanism: from dislocation motion (SFE > 45 mJm^{-2}) to TWIP (45 mJm^{-2} > SFE > 18 mJm^{-2}) and TRIP (SFE < 18 mJm^{-2}) [5,9].

SFE decreases as the deformation temperatures drops [4,5,11], which is closely related with the mechanical performance. The high SFE at high temperatures can limit the strain hardening effect due to the inability to activate multiple deformation mechanisms [5,12]. While SFE when dropped to too low at low temperatures (e.g. SFE < 18 mJm^{-2} with TRIP effect), sometimes, can be detrimental to the mechanical performance, e.g., yield strength (YS) and ductility [11,13,14]. Wang et al. [14] indicated that the abundance of strain-induced martensite phases can reduce the YS due to the imposed pre-yield transformation

stress. Saeed-Akbari [13] showed that when SFE dropped from 35 mJm^{-2} to ~0 mJm^{-2}, the elongation to fracture of high Mn steels was significantly decreased from 0.28 to 0.08. Notably, there is also a need to avoid the formation of ferromagnetic martensite phases during loading, particularly for applications in superconducting magnets. Therefore, precisely controlling the SFE to a desirable range is critical in tailoring the strengthening mechanisms and designing the mechanical performance for specific working conditions, e.g., cryogenic applications. This requires the combination of effective SFE-adjusting methods and accurate SFE measurement. *In situ* neutron diffraction coupled with tensile testing at cryogenic temperatures, which can be used to accurately depict SFE evolution as a function of temperature [11,15], is a powerful tool to study the relationship between mechanical responses and deformation mechanisms of high Mn steels [4].

Recently, Cu alloying is emerging as a low-cost and high effective method to adjust the SFE of TWIP steels [16–20]. Dumay et al. [10] indicated that the SFE of the high-Mn steel can be increased by 1.52 mJm^{-2} for 1 wt.% of Cu addition. The effects of Cu on mechanical performance, however, are still under debate. Gonzalez et al. [21] found out that the uniform elongation of an austenite stainless steel is improved and the martensite formation is suppressed by Cu addition. Lee et al. [17] indicated that the addition of Cu has almost no influence on the YS of the Fe-Mn-C-Al steel, while the kinetics of twin formation was suppressed and the ultimate tensile strength (UTS) was decreased. Peng et al. [18] showed that the YS of Fe-20Mn-1.3C increased from 470 MPa to 538 MPa after adding 3 wt.% Cu due to the solid solution strengthening. Kim et al. [20] indicated that 1 wt.% of Cu addition can improve the YS of Fe-22Mn-0.45C-1Al steel at 293 and 77 K but decrease the UTS slightly. Choi et al. [22] found out that both YS and UTS can be decreased with increasing Cu content. Therefore, it is important to further shed a light on the effects of Cu on SFE, deformation mechanisms, and mechanical behaviors, especially in cryogenic conditions where the effects of Cu addition [22] have rarely been explored.

Herein, we investigated the deformation mechanisms and mechanical properties of two high Mn steels with different Cu concentrations (Fe-24Mn-4Cr-0.5C and Fe-24Mn-4Cr-0.5C-1Cu, weight percent and hereafter) at low temperatures (293, 173, and 77 K). The *in situ* neutron diffraction and tensile tests were performed to track the microstructure

evolution and mechanical responses during deformation. The neutron diffraction spectra analysis allowed us not only to determine key materials parameters, e.g., lattice parameter, elastic moduli, single-crystal elastic constants, and SFE as a function of temperature, but also to observe the evolution of multiple microstructural features during straining, such as lattice strain, stacking fault probability (SFP), and dislocation density. Meanwhile, post-mortem TEM characterization was performed on the fractured samples to observe the deformed microstructures. The strengthening contributions from different resources, including grain boundaries, dislocations, twins, and martensite phases were then calculated and compared. Based on these results, the effects of Cu addition on SFE, deformation mechanisms, and mechanical performance at the low-temperature range were then discussed in detail.

2. Materials and methods

2.1 Materials processing

Two high-Mn steels with different Cu concentrations, Fe-24Mn-4Cr-0.5C and Fe-24Mn-4Cr-1Cu-0.5C wt.% steels (marked as 0-Cu and 1-Cu steels, respectively), were provided by Baowu steel company. High purity metals (purity ≥ 99.9%) were melted to cast ingots by vacuum induction melting and casting. The cast ingot was cut into a dimension of 120 mm (thickness) × 180 mm (width) × 240 mm (length). After homogenization treatment at 1473 K for 48 h, the ingot was hot rolled at 1200 K to a thickness of 17 mm (~86% of reduction) via 7 passes, followed by cooling down to room temperature by water quenching.

2.2 *In situ* neutron diffraction

In situ time-of-flight neutron diffraction and tensile tests were performed at the beamline of ENGIN-X, ISIS spallation neutron source, the Rutherford Appleton Laboratory, UK. The schematical illustration of the *in situ* neutron diffraction experiments can be seen in Ref. [4]. Before reaching the tensile bars, the incident neutron beam with a continuous range of speed was modified by the moderator and slits (with a size of 4 × 4 mm^2). Two signal detector banks (tensile and side) were mounted perpendicularly to the incident beam,

collecting the diffracted neutrons from crystallographic planes subjected to tensile and compressive stress, respectively. The size of the diffracted neutron beams was defined by the two collimators, deciding the scattering gauge volume of 4 × 4 × 4 mm^3. Dog-bone tensile bars with a gauge volume of Φ 8 × 32 mm^3 (see details at Ref. [4]) as well as an Instron stress rig were mounted 45° to the incident beam. Tensile tests were carried out with a strain rate of 9×10^{-4} s^{-1} in a high-vacuum (< 10^{-5} Pa) chamber equipped with built-in heaters and a liquid helium circulation system to perform cryogenic deformation. The high-vacuum and low-temperature environments were stabilized for 30 mins before straining. The tensile tests were paused for the sequential signal collection, which consumes 20 mins between tensile loading intervals. An extensometer was used to measure the strain. Before tensile tests, a standard CeO_2 sample was used to calibrate the experimental geometry and subtract the instrumental broadening effect.

The single peak-fitting was performed with pseudo-Voigt function allowing the determination of peak intensity, full width at half maximum (FWHM), peak position, and lattice parameter (a). The Rietveld refinement was performed on the TOPAS software (Coelho Software, Australia) was used to determine fraction of different phases formed during tensile testing. The lattice strain (ε_{hkl}^{exp}) is defined as the change of the spacing distance of a given crystallographic plane in response to external stress. It then can be determined with:

$$\varepsilon_{hkl}^{exp} = \frac{d_{hkl} - d_{hkl}^{0}}{d_{hkl}^{0}} \quad (1)$$

, where d_{hkl}^{0} and d_{hkl} is the inter-planar distance of $\{hkl\}$ grain plane without stress and under different stress conditions, respectively. The approaches we used to calculate the stacking fault probability (SFP), stacking fault energy (SFE), and dislocation density can be found in Ref. [4].

2.3 SFE prediction based on thermodynamics

The SFE of the two steels were explored with both experimental measurement based on neutron diffraction (see details at Refs. [4,11]) and theoretical calculations (based on thermodynamics).

The thermodynamic modeling approach of calculating the SFE was first proposed by Olson and Cohen [23]. Formed by the dissociation of perfect dislocations, the stacking faults can disrupt the normal sequence of the {111} plane. Therefore, this model treats the stacking faults as a thin layer of HCP plate separating the normal stacking matrix into two parts. The ideal SFE can then be expressed with [23]:

$$SFE = 2\rho\Delta G^{\gamma\to\varepsilon} + 2\sigma, \tag{2}$$

, where ρ is the molar surface density along {111} planes, $\Delta G^{\gamma\to\varepsilon}$ is the molar Gibbs energy of the phase transformation ($\gamma \to \varepsilon$), and σ = 5 mJm^{-2} is the interfacial energy per unit area of phase boundary as its value is generally taken between 5 and 15 mJm^{-2} for transition metals [24]. The molar surface density ρ can be calculated with the lattice parameter a and Avogadro's constant N:

$$\rho = \frac{4}{\sqrt{3}}\frac{1}{a^2 N}. \tag{3}$$

In this model, the steels were assumed to be in a regular solid solution state, the substitutional atoms were at the lattice sites while interstitial atoms locate at the octahedral site of the FCC and HCP lattice. $\Delta G^{\gamma\to\varepsilon}$ in Eq. (11) includes the chemical contribution of all substitution elements to Gibbs free energy of $\gamma \to \varepsilon$ phase transformation ($\Delta G^{\gamma\to\varepsilon}_{FeMnX}$), the contribution of interstitial carbon ($\Delta G^{\gamma\to\varepsilon}_{FeMnX/C}$), and atom magnetic contribution of Gibbs free energy ($\Delta G^{\gamma\to\varepsilon}_{mg}$) originating from the Néel transition (paramagnetic to antiferromagnetic) [9]:

$$\Delta G^{\gamma\to\varepsilon} = \Delta G^{\gamma\to\varepsilon}_{FeMnX} + \chi_C \Delta G^{\gamma\to\varepsilon}_{FeMnX/C} + \Delta G^{\gamma\to\varepsilon}_{mg}, \tag{4}$$

in which χ_i is the molar fraction of each alloying element.

According to Ref. [5], the chemical contribution $\Delta G^{\gamma\to\varepsilon}_{FeMnX}$ and the contribution from carbon addition $\Delta G^{\gamma\to\varepsilon}_{FeMnX/C}$ can be calculated with:

$$\begin{aligned}\Delta G^{\gamma\to\varepsilon}_{FeMnX} = {} & \chi_{Fe}\Delta G^{\gamma\to\varepsilon}_{Fe} + \chi_{Mn}\Delta G^{\gamma\to\varepsilon}_{Mn} + \chi_{Cr}\Delta G^{\gamma\to\varepsilon}_{Cr} + \chi_{Cu}\Delta G^{\gamma\to\varepsilon}_{Cu} + \chi_C\Delta G^{\gamma\to\varepsilon}_{C} \\ & \chi_{Fe}\chi_{Mn}\Delta\Omega^{\gamma\to\varepsilon}_{FeMn} + \chi_{Fe}\chi_{Cr}\Delta\Omega^{\gamma\to\varepsilon}_{FeCr} + \chi_{Fe}\chi_{Cu}\Delta\Omega^{\gamma\to\varepsilon}_{FeCu} + \chi_{Fe}\chi_C\Delta\Omega^{\gamma\to\varepsilon}_{FeC}\end{aligned} \tag{5}$$

$$\Delta G_{FeMnX/C}^{\gamma\to\varepsilon} = \frac{1246}{\chi_C}\left(1 - e^{-24.29\chi_C}\right) - 17.175\chi_{Mn} \tag{6}$$

The magnetic contribution to the Gibbs free energy change $\Delta G_{mg}^{\gamma\to\varepsilon}$ was calculated with

$$\Delta G_{mg}^{\gamma\to\varepsilon} = G_{mg}^{\varepsilon} - G_{mg}^{\gamma}, \tag{7}$$

where $G_{mg}^{\varphi}(\varphi = \gamma, \varepsilon)$ is represented by

$$\Delta G_{mg}^{\varphi} = RT\ln(1+\beta^{\Phi}) f^{\Phi}(\tau^{\Phi}), \mu = \gamma, \varepsilon \tag{8}$$

where R is the gas constant, T is the temperature, β^{Φ} is the magnetic moment of the phase φ divided by the Bohr magneton μ_B, and $f^{\Phi}(\tau^{\Phi})$ is a polynomial function of the scaled Néel temperature $\tau^{\Phi} = T / T_{Néel}$ of phase φ [25]. The magnetic moment of the γ phase was determined with the simple mixing rule of the magnetic moment of each element:

$$\beta^{\gamma} = \chi_{Fe}\beta_{Fe} + \chi_{Mn}\beta_{Mn} - \chi_{Cr}\beta_{Cr} - \chi_{Fe}\chi_{Mn}\beta_{FeMn} - \chi_C\beta_C, \tag{9}$$

in which β_{Fe}=0.7, β_{Mn}=0.62, β_{Cr}=0.8, β_{FeMn}=0.64, and β_C=4 [10,25] are empirical values for the pure elements' magnetic moments. The magnetic moments of the martensite phase ε can be calculated with the following equation [10]:

$$\beta^{\varepsilon} = \chi_{Mn}\beta_{Mn} - \chi_C\beta_C \tag{10}$$

The magnetic transition temperature of each phase $T_{Néel}^{\Phi}$ was calculated with empirical expressions in Refs. [26]:

$$T_{Néel}^{\gamma} = 251.71 + 681\chi_{Mn} - 272\chi_{Cr} - 1740\chi_C \tag{11}$$

$$T_{Néel}^{\varepsilon} = 580\chi_{Mn} \tag{12}$$

According to Ref. [27], the term $f^{\Phi}(\tau^{\Phi})$ in Eq. (8) can be expressed with the following equation:

$$f^{\Phi}(\tau^{\Phi}) = \begin{cases} 1 - \left[\dfrac{79\tau^{-1}}{140p} + \dfrac{474}{497}\left(\dfrac{1}{p} - 1\right)\right]\left(\dfrac{\tau^3}{6} + \dfrac{\tau^9}{135} + \dfrac{\tau^{15}}{600}\right)\Big/ D & (\tau \le 1) \\ -\left[\dfrac{\tau^{-5}}{10} + \dfrac{\tau^{-15}}{315} + \dfrac{\tau^{-25}}{1500}\right]\Big/ D & (\tau > 1) \end{cases} \tag{13}$$

where p = 0.28 and D = 2.342456517 for FCC and HCP phases [28].

Table 1 Numerical values and functions used for thermodynamical calculations

Parameter	Functions [J·mol^{-1}]	Ref.
$\Delta G_{Fe}^{\gamma\to\varepsilon}$	$-2243.38+4.309T$	[9]
$\Delta G_{Mn}^{\gamma\to\varepsilon}$	$-1000.00+1.123T$	[9]
$\Delta G_{Cr}^{\gamma\to\varepsilon}$	$-1370.00-10T$	[29]
$\Delta G_{Cu}^{\gamma\to\varepsilon}$	$600+0.2T$	[30]
$\Delta G_{C}^{\gamma\to\varepsilon}$	–22166	[30]
$\Delta\Omega_{FeMn}^{\gamma\to\varepsilon}$	$2873+717(\chi_{Fe}-\chi_{Mn})$	[31]
$\Delta\Omega_{FeCr}^{\gamma\to\varepsilon}$	2095	[32]
$\Delta\Omega_{FeCu}^{\gamma\to\varepsilon}$	7506	[10]
$\Delta\Omega_{FeC}^{\gamma\to\varepsilon}$	42500	[25]

2.4 Post-mortem microstructure characterization

The as-received samples were metallographically polished before the microscopic characterization. The electron backscatter diffraction (EBSD) was performed on an HKL EBSD detector based on a field emission gun scanning electron microscope (FEI Sirion 200), which was set to a voltage of 20 kV, current of 25 nA, and step size of 0.5 μm. The EBSD data analysis was performed with HKL Channel 5 software, during which the misorientation angles less than 2° were ignored to avoid ambiguity. The samples for microscope observation were sectioned from the fractured sample with electrical discharge machining. For the transmission electron microscope (TEM) and scanning TEM (STEM) observation, thin foils were mechanically polished to a thickness of ~60 μm before the twin-jet electropolishing with a current of 150 mA in a solution of 5% perchloric acid and 95% methanol after cooling down to -30℃. The bright-field TEM observation was carried out on a Technai G2 F30 microscope with an accelerate voltage of 300 kV. The high-resolution TEM images (HRTEM) and atomic-resolution high-angle annular dark-field STEM (HAADF-STEM) images were collected on an aberration-corrected Titan 60-300 microscope. The collection half-angle of the HAADF detector ranging from 60 to 290 mrad was used, with the convergence half-angle of 21.4 mrad, giving a probe size of ~1.2 Å.

3. Results

3.1 Microstructure of the as-fabricated steels

The as-fabricated 0-Cu and 1-Cu steel shared very similar microstructure thus only the images of the 0-Cu steel were presented here. Fig. 1a shows the typical EBSD inverse pole figure (IPF) of the virgin 0-Cu steel. Most of the grains were large equiaxed grains after the hot rolling. The mean grain size of 14.5±1.3 μm was determined by the line-intercept method excluding twin boundaries (TBs). The low-angle grain boundaries (LAGBs, $2° \leq \theta \leq 15°$), high-angle grain boundaries (HAGBs, $15° < \theta$), and Σ3{111} TBs of Fig. 1a were marked and overlapped with the band contrast map in Fig. 1b. The LAGBs have a relatively low fraction of 13.8% accompanied by 86.2% of HAGBs. Fig. 1b shows the high density of Σ3{111} annealing TBs, which contributed to the high fraction of HAGBs at around 60° (Fig. 1c). In addition to the TBs, the grain misorientation distribution followed a pattern of random misorientation distribution (Fig. 1c). A typical bright-field TEM image is shown in Fig.1d, showing that the microstructure consists of dense-dislocation and dislocation-free zones. The dislocation cells and dislocation entanglements can be observed in the dense dislocation zone. The dislocation free zone mainly consists of equiaxed recrystallized grains and parallel-sided annealing twins, which initialized from the grain boundaries and expanded into the grain interior. The {100}, {110}, and {111} pole figures of the as-fabricated 0-Cu steel were shown in Fig. 1d, revealing an almost random texture with a maximum peak intensity of 2.77 multiples of random distribution (MRD) in the {111} pole figure.

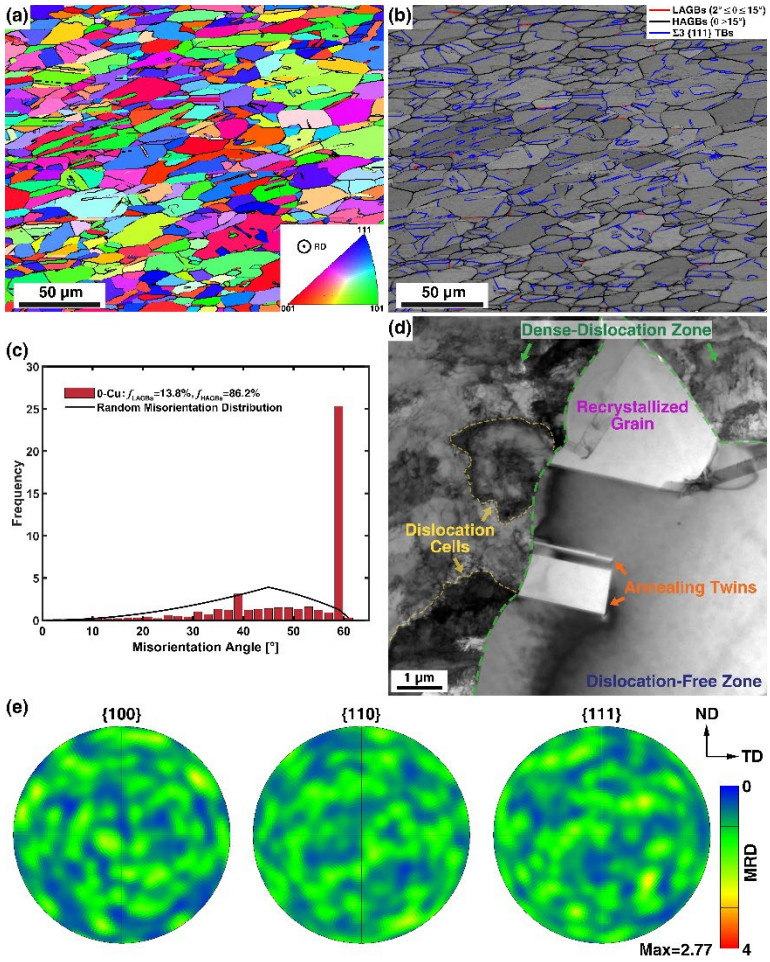

Fig. 1 Initial microstructure of the 0-Cu steel: (a) EBSD inverse pole figure (IPF) map, (b) Band contrast map overlapped with boundaries map, (c) sample and random misorientation, (d) typical bright-field TEM image. RD, TD, and ND denote the rolling, transverse, and normal direction, respectively. MRD denotes the multiples of random distribution.

3.2 Tensile properties

The engineering stress-strain curves of the 0-Cu and 1-Cu steels deformed at 293, 173, and 77 K were shown in Fig. 2a and 2b, respectively. The mechanical properties of the 0-Cu, 0.5-Cu (Fe-24Mn-4Cr-0.5Cu-0.5C, from Ref. [4]), and 1-Cu steel were compared in Fig. 2c. At 293 K the YS and UTS of the 0-Cu steel were 336 MPa and 930 MPa, respectively (Table. 2). As the deformation temperature decreased, both YS and UTS witnessed a substantial and almost linear increase to 700 MPa and 1361 MPa, respectively. The ductility, however, decreased linearly from an ultrahigh value of 104% at 293 K to 68% at 77 K. The mechanical property of the 0.5-Cu and 1-Cu steel showed very similar

temperature dependence. The Cu addition witness a steady increase in YS as the 1-Cu steel showed higher YS (~100 MPa) but slightly lower UTS (less than 50 MPa) than the 0-Cu steel at all three temperatures. Besides, the uniform elongation of the 1-Cu steel was maintained at a very high level (~0.65) at the low-temperature range.

Defined as the derivative of true stress *v.s.* true strain, $d\sigma/d\varepsilon$, the strain hardening rate (SHR) of the two steels during deforming at different temperatures are plotted as a function of true stress in Fig. 2c (0-Cu) and 2d (1-Cu), respectively. For the 0-Cu steel, the SHR curves at the three deformation temperatures shared a similar pattern and they can be categorized into three stages (separated with dash lines in Fig. 2c). Initially, the SHR curve dropped rapidly (Stage I), followed by a stable period during which the SHR increased slightly (Stage II), indicating the emergence of new and steady strengthening effects. At the last stage (Stage III), the SHR curve dropped again until fracture. The SHR curves of the 1-Cu steel (Fig. 2d) are also temperature-dependent and can also be divided into three stages. At 293 K, the SHR curve kept decreasing during straining, but the dropping rate varied with stages. When decreasing temperature to 173 and 77 K, the strengthening effects were improved significantly and both SHR curves show an increasing trend at Stage II while gradually decrease during the following Stage III.

Table 2 Mechanical properties of the steels at different temperatures

Steels	0-Cu			0.5-Cu			1-Cu		
Temperature [K]	293	173	77	293	173	77	293	173	77
YS [MPa]	336	539	700	442	625	760	457	643	793
UTS [MPa]	930	1159	1361	918	1107	1312	876	1115	1323
Uniform elongation [%]	84	72	68	72	54	56	63	70	64

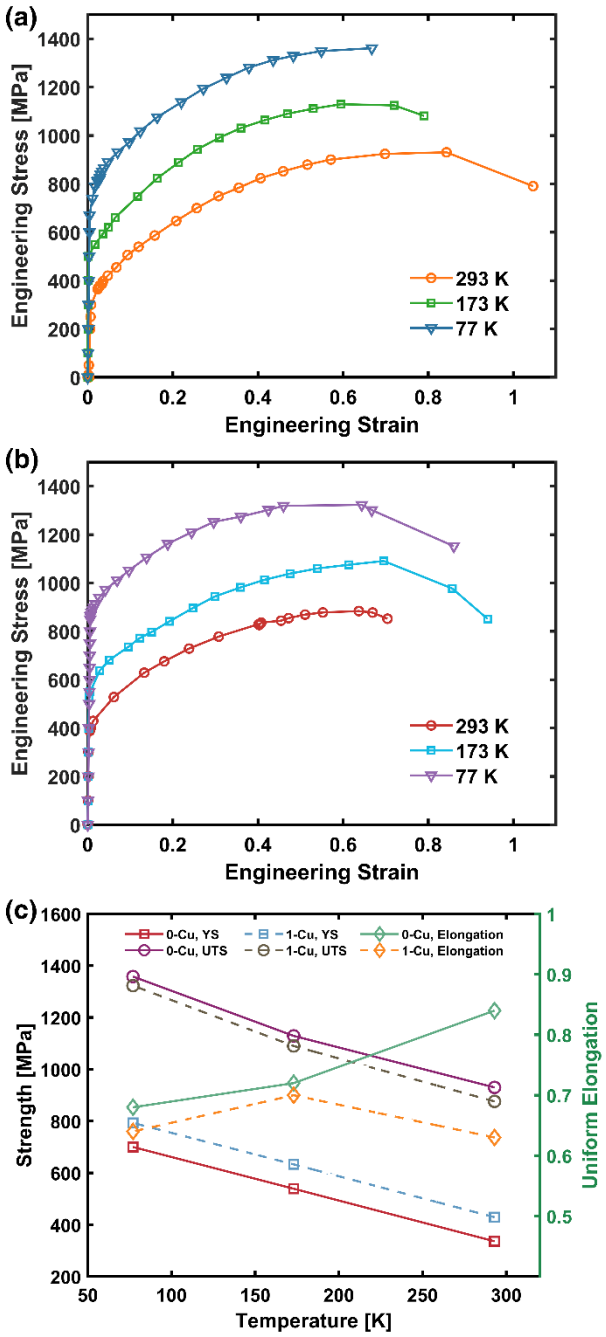

Fig. 2 Mechanical performance of the two high Mn steels at 293, 173, and 77 K: engineering stress strain curves of the (a) 0-Cu and (b) 1-Cu alloy, respectively. (c) The evolution of mechanical properties with deformation temperature.

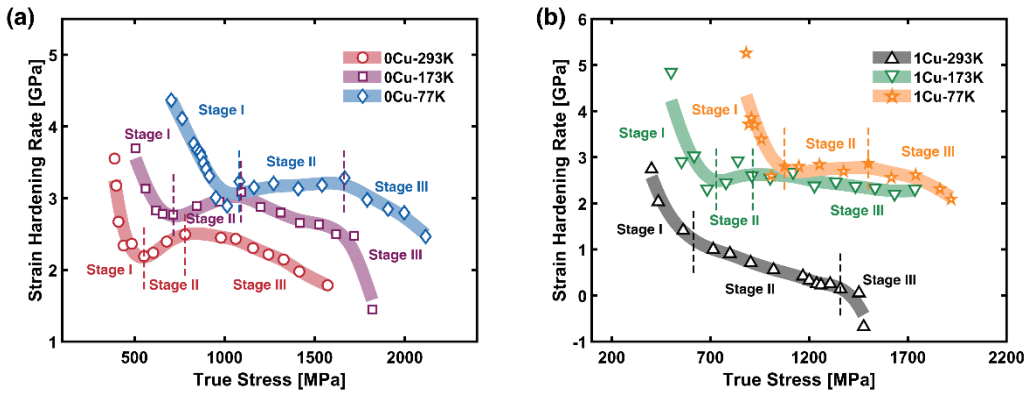

Fig. 3 Strain hardening rate (SHR) curves of the (a) 0-Cu and (b) 1-Cu alloy during deforming at 293, 173 and 77 K.

3.3 *In situ* neutron diffraction spectra

Fig. 4 shows the *in situ* neutron diffraction patterns (tensile direction) of the two steels collected during tensile tests at different temperatures. The two steels maintained a single FCC structure as they are cooled down to cryogenic temperatures as only five diffraction peaks of FCC phase were identified. During deformation, the FCC structure of both steels was stable at 293 K as no other peaks appeared. While deforming the 0-Cu steel at 77 K, a new diffraction peak appeared after yield point and its intensity grew stronger with straining (marked with a green line in Fig. 4b). This peak was identified as the $(10\bar{1}1)$ peak of the HCP phase [4]. This indicates the low temperature reduced the stability of the original FCC phases and strain-induced phase transformation from FCC to HCP occurred. A similar phenomenon was observed when deforming the 1-Cu steel at 77 K, but the new peak has a very weak peak intensity, indicating that a trace amount of the newborn HCP phases was produced.

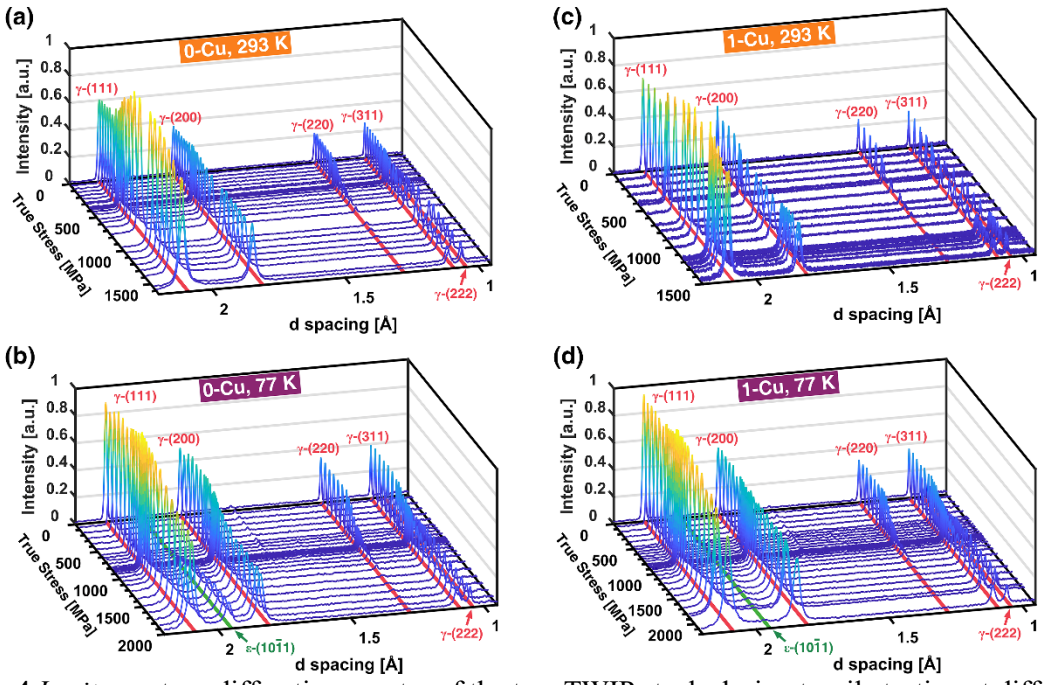

Fig. 4 *In situ* neutron diffraction spectra of the two TWIP steels during tensile testing at different temperatures: (a) 0-Cu, 293 K; (b) 0-Cu 77 K; (c) 1-Cu, 293 K; (d) 1-Cu, 77 K.

The macroscopic and *hkl*-specific elastic moduli were measured by analyzing the neutron diffraction patterns. The macroscopic Young's modulus (E) was determined by linear fitting the applied stress as a function of true strain at the elastic stage. The lattice parameters of the two steels are very close (3.615 Å for 0-Cu and 3.616 Å for 1-Cu) and they both decreased almost linearly with the decrease of temperature (Table. 3). With the increase of true stress, the lattice parameter obtained from tensile and side signals increased and decreased almost linearly at the elastic stage, respectively. The macroscopic Poisson's ratio (v) was determined by the ratio of the two fitted lines. Then the bulk shear modulus (G) can be obtained via $G=E/(1+v)$. The lattice strain evolution of four grain families ({111}, {200}, {220}, and {311}) along tensile and side direction at different temperatures was calculated with Eq. (1) and shown in Fig. 5. The *hkl*-specific lattice strain also increased/decreased linearly with stress before yielding and showed varied yield behaviors. With linear fitting the data at the elastic stage, their slopes determine the *hkl*-specific diffraction elastic moduli (E_{111}, E_{200}, E_{220}, and E_{311}). The ratio of elastic moduli between the tensile and side direction determined the Poisson's ratio of different grain families (v_{hkl}). Among all the orientations, E_{111} and E_{200} show the highest and lowest values, respectively.

Meanwhile, reducing the temperature can increase the stiffness of the steel. With the decrease of temperature, the shear modulus and all elastic moduli (except E_{311}, which remained at the same level) of the two steels increased. The Poisson's ratio showed a decreasing trend (Table. 3). During the following plastic deformation, the lattice strain increased non-linearly with the applied stress since the stress gradually transferred from some stiff orientations, e.g., <220>//LD (loading direction) to some compliant orientations, e.g., <200>//LD.

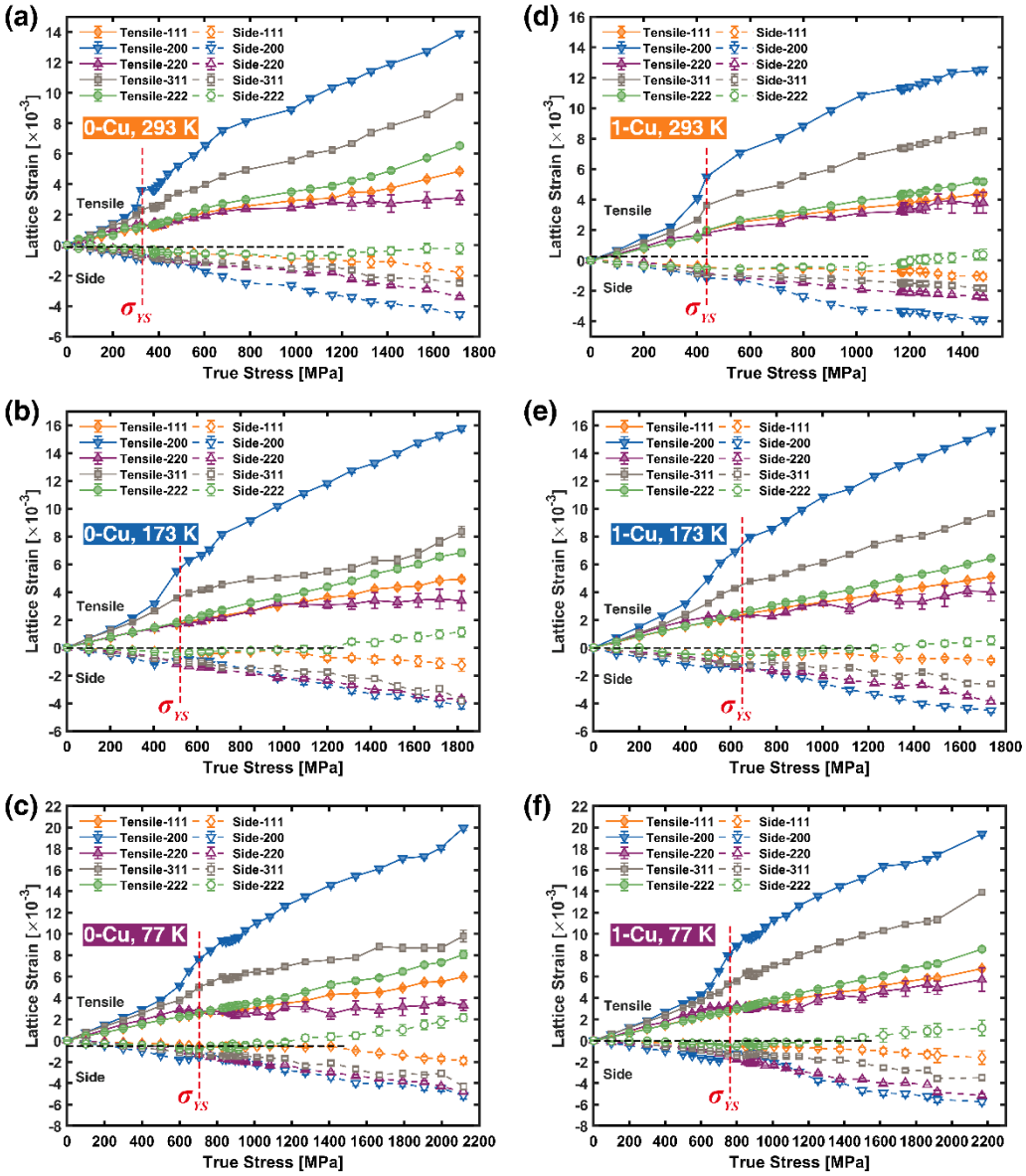

Fig. 5 Lattice strain evolution of five crystallographic planes ({111}, {200}, {220}, {311}, and {222}) of two TWIP steels (0-Cu and 1-Cu) during deforming at different temperatures: (a) 0-Cu, 293 K; (b) 0-Cu, 173 K; (c) 0-Cu 77 K; (d) 1-Cu, 293 K; (e) 1-Cu, 173 K; (f) 1-Cu, 77 K.

Fig. 6 shows the elastic moduli of grains with different orientations plotted as a function of the elastic anisotropy factor and the fitted lines with the Voigt, Reuss, and Kroner models at 293 K. The details of the calculation can be found at Ref. [33]. The fitting results indicate that the self-consistent Kroner model has the best agreement with the experimental results as compared with the Voigt and Reuss model. According to Refs. [34], these two theoretical models were generally used to estimate the upper and lower bounds of the diffraction and macroscopic elastic moduli as they only assume all grains are subjected to a homogeneous strain (Voigt) or stress (Reuss) but failed to meet the equilibrium (Voigt) and continuity (Reuss) at grain boundaries during loading. The *hkl*-specific diffraction elastic moduli obtained from neutron diffraction were used to determine the single-crystal elastic constants (C_{11}, C_{12}, and C_{44}) with the Kroner's model at different temperatures (Table. 3). The result shows that 1-Cu steel has higher C_{11} than that of 0-Cu steel at the three temperatures, but there is no significant difference in C_{12} and C_{44} between the two compositions. The single-crystal elastic constants were used for SFE (Section 3.4) and dislocation density calculations (Section 3.5).

Table 3 Multiple properties of the 0-Cu and 1-Cu steel at 293, 173, and 77 K

Steel	0-Cu			1-Cu		
Temperature [K]	293	173	77	293	173	77
a [Å]	3.615	3.611	3.610	3.616	3.612	3.611
E [GPa]	191.3	192.1	193.4	191.5	191.1	193.6
E_{111} [GPa]	280.1	282.5	283.5	259.1	272.6	279.3
E_{200} [GPa]	126.4	129.0	133.2	135.1	136.7	138.5
E_{220} [GPa]	202.0	202.8	208.2	207.6	203.4	205.3
E_{311} [GPa]	157.2	156.2	156.7	152.1	156.0	156.6
G [GPa]	73.35	75.45	77.17	75.57	76.20	78.76
v	0.304	0.273	0.253	0.267	0.254	0.229
v_{111}	0.231	0.225	0.223	0.241	0.226	0.215
v_{200}	0.375	0.368	0.375	0.371	0.380	0.367
v_{220}	0.295	0.312	0.300	0.336	0.337	0.332
v_{311}	0.329	0.306	0.305	0.325	0.321	0.323
C_{11} [GPa]	223	227	231	240	243	250
C_{12} [GPa]	170	172	175	182	186	190
C_{44} [GPa]	129	132	132	128	128	134

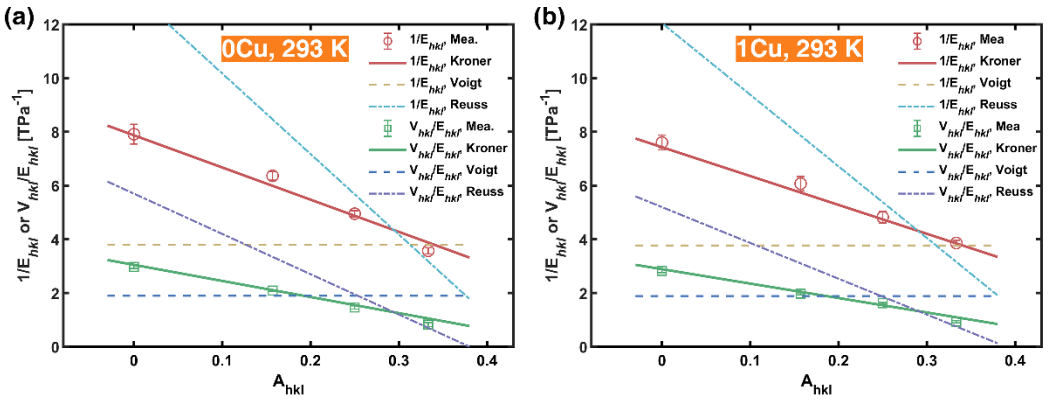

Fig. 6 Plots of the reciprocal diffraction moduli ($1/E_{hkl}$ and ν/E_{hkl}) of differently oriented crystals as a function of the elastic anisotropy factor ($A_{hkl} = \left(h^2k^2 + h^2l^2 + k^2l^2\right) \Big/ \left(h^2 + k^2 + l^2\right)^2$) and the fitting results based on Kroner, Voigt, and Reuss model of the (a) 0-Cu and (b) 1-Cu steel at 293 K.

3.4 SFE evolution

The lattice strain of {111} and {222} grain families increased with strain but a growing split between them was observed (Fig. 7). This is a signature of the formation of stacking faults, which causes extra strain and separates lattice strain curves from different orders of Miller indices [15]. Stacking fault probability (SFP), a parameter that measures the amount of formed stacking faults, can thus be determined by measuring the separating distance between the lattice strain curves from two consecutive grain planes. The detailed calculation procedure can be found at Refs. [4,11]. In Fig. 7, the lattice strain evolution of {111} and {222} grain families and the calculated SFP of the two steels were plotted against true strain at different temperatures. At the low strain regime, the SFP fluctuates at around 0 and the negative value was caused by the small errors introduced during peak fitting. SFP increases almost linearly with true strain and a linear function was applied to depict the stacking fault multiplication during straining. After linear fitting, the slopes ($\partial SFP/\partial\varepsilon$) of these lines define the speed of stacking faults production (Fig. 7) [4]. The low temperature can effectively promote the SF formation and increase $\partial SFP/\partial\varepsilon$. The $\partial SFP/\partial\varepsilon$ of the 0-Cu steel is 4.63×10^{-2} at 293 K and almost linearly increased to 8.41×10^{-2} at 77 K (Fig. 8). The 1-Cu steel showed a very similar pattern but with a lower increase rate, which is 3.39×10^{-2} at 293 K and 7.0×10^{-2} at 77 K.

The SFE can then be calculated based on the SFP and details can be found at Refs. [4,11]. It is worth noting that when SFE becomes negative and the balance between SFE and the elastic repulsive force between partial dislocations breaks down, the traditional experimental measurement of the SFE is no longer suitable [35]. The evolution of $\partial SFP/\partial\varepsilon$ and measured SFE were plotted as a function of deformation temperature in Fig. 8. For the 0-Cu steel, its SFE started from 26.8±0.5 mJm^{-2} at 293 K and almost linearly decreased to 15.5±1.7 mJm^{-2} at 77 K. The 1-Cu steel showed a higher level of SFE (33.8±1.8 mJm^{-2} at 293 K, and 20.7±0.7 mJm^{-2} at 77 K), ~5-7 mJm^{-2} higher than that of the 0-Cu steel within the whole temperature range. The slopes of the SFE-temperature curves also showed a very close value with 0.056±0.006 $mJm^{-2}K^{-1}$ for the 0-Cu steel and 0.059±0.008 $mJm^{-2}K^{-1}$ for the 1-Cu steel. The values are also very close to 0.061 $mJm^{-2}K^{-1}$ in the Fe-24Mn-4Cr-1Cu-0.5C steel reported in Ref. [4]. According to the SFE-deformation mechanism map overlapped in Fig. 8, the SFE of the 0-Cu steel stayed at the twinning-dominant region at ~125-373 K, while it dropped to the phase transformation region at 77 K. The SFE of the 1-Cu steel showed similar temperature dependence but it remained at the twinning zone at the three tested temperatures. This indicates the transition of the dominant deformation mechanism, which agrees well with the diffraction results shown in Fig. 4, where observable diffraction peaks of $(10\bar{1}1)$ of HCP phase were formed when deforming the 0-Cu steel at 77 K, while only trace amount of HCP phase were formed in the 1-Cu steel at 77 K.

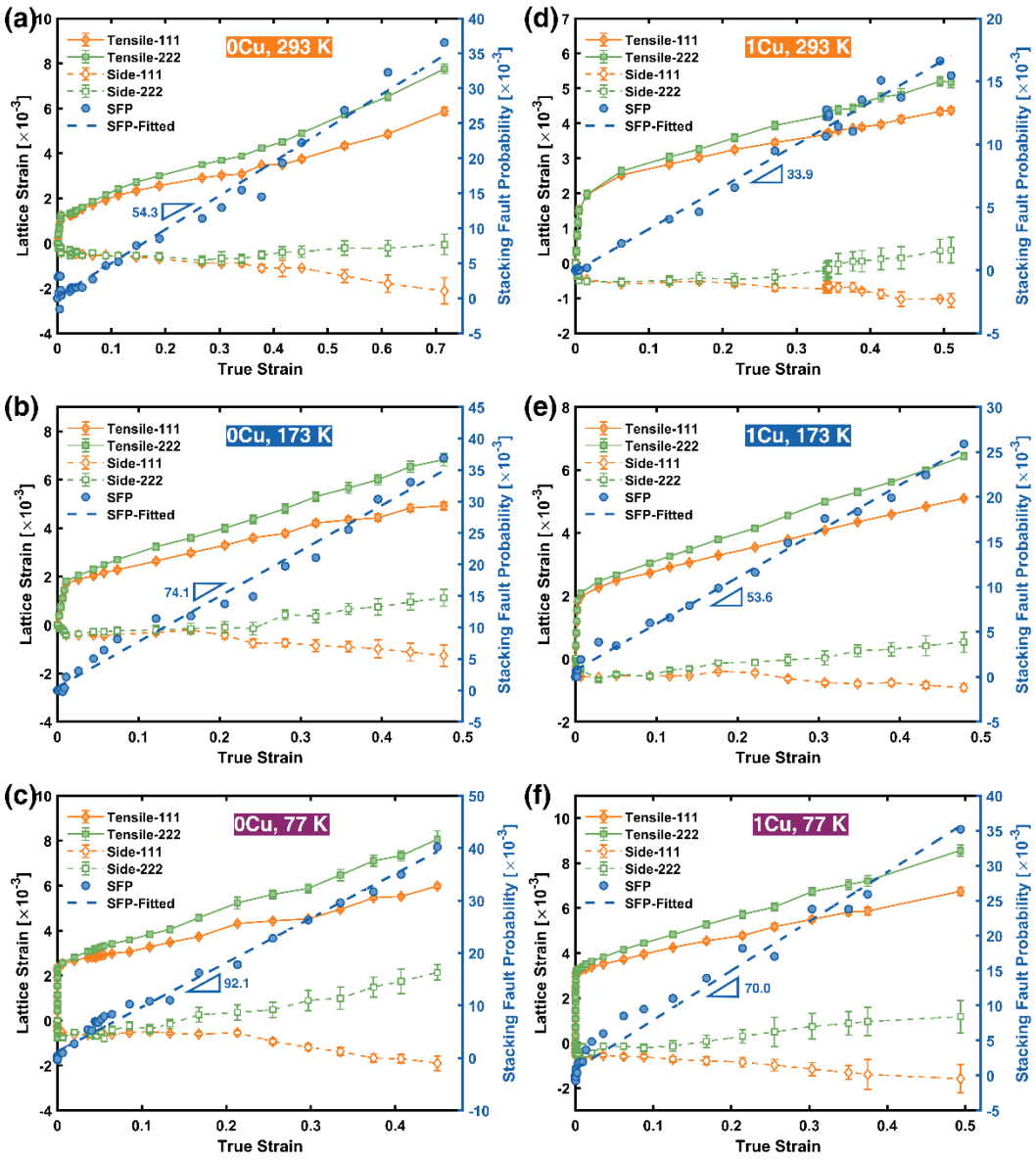

Fig. 7 Lattice strain evolution of {111} and {222} grain planes along tensile and side direction and the corresponding stacking fault probability change of the two TWIP steels during deforming at different deformation temperatures: (a) 0-Cu, 293 K; (b) 0-Cu, 173 K; (c) 0-Cu 77 K; (d) 1-Cu, 293 K; (e) 1-Cu, 173 K; (f) 1-Cu, 77 K.

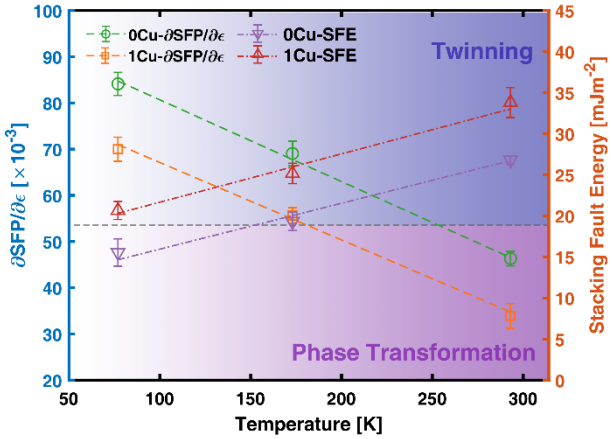

Fig. 8 Temperature dependence of stacking fault probability (SFP) and stacking fault energy (SFE) of the two TWIP steels (measured with neutron diffraction patterns).

Besides, the measured SFE shows an acceptable match with the thermodynamical prediction (Table. 4). The disparity between the two SFE-determination methods is relatively small (~2 mJm^{-2}) except for the results of the 1-Cu steel at 293 K (~5 mJm^{-2}). The difference between theoretical calculation and experimental measurement can be originated from that the SFE can be influenced by several factors (e.g., strain rate [5] and grain size [36]). These factors, however, were not considered in the thermodynamical modeling.

Table. 4 Temperature-dependent SFE of the 0-Cu and 1-Cu steels determined with thermodynamics and neutron diffraction

Steels	Temperature [K]	SFE [mJm^{-2}] (Neutron Diffraction)	SFE [mJm^{-2}] (Thermodynamics)
0-Cu	293	26.8±0.5	26.4
	173	19.3±1.1	20.3
	77	15.5±1.7	16.6
1-Cu	293	33.8±2.2	28.8
	173	25.2±1.2	23.0
	77	20.7±0.7	19.2

3.5 Dislocation density calculation

To analyze the strengthening contribution of forest hardening effects, it is necessary to quantitatively determine the evolution of dislocation density during straining. The dislocation density was calculated with the neutron diffraction patterns based on the modified Williamson-Hall model [37]. The detailed calculation process can be found in Ref. [4]. The dislocation density evolution of the two steels at 293, 173, and 77 K was

plotted with respect to true strain in Fig. 9. As shown in Fig. 9a, at three deformation temperatures, the dislocation density of the two steels was ~7×10^{13} m^{-2}, and it increased almost linearly with the increase of true strain after yielding. The decrease of deformation temperature accelerated dislocation accumulation: at a true strain of 0.5, the dislocation density at 293 K reached ~1.00×10^{15} m^{-2} and it increased to ~1.52×10^{15} m^{-2} at 173 K and ~2.41×10^{15} m^{-2} at 77 K. Similar phenomena was also observed in the 1-Cu steel.

The varied increasing speeds of dislocation density of the two steels originate from the varied SFE and deformation temperature. The increased dislocation density is the concurrent result of dislocation generation and dynamic recovery [38]. Due to the low SFE, the perfect dislocations tend to slip on parallel slip planes or dissociate into two Shockley partials with stacking faults existing in between. Dense planar dislocation arrays and stacking faults on parallel {111} slip planes are thus highly expected. These microstructures can serve as effective dislocation barriers and contribute dislocation accumulation. On the other hand, the dynamic recovery can also be impeded by the decrease of temperature. When the temperature decreases to below 0.3 T_m (T_m: melting temperature), the dynamic recovery mainly relies on dislocation cross slip [39]. The decrease of temperature can impede cross slip of dislocation by reducing the thermal activation and creating more extended dislocation cores. [36]. Hence, the growth speeds of dislocation density increased as the deformation temperature was decreased.

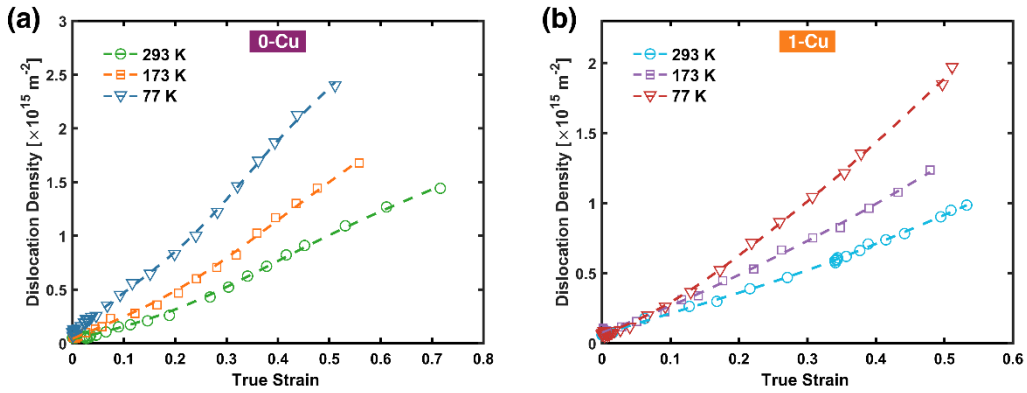

Fig. 9 The evolution of dislocation density of the two high Mn alloys during deforming at 293, 173, and 77 K: (a) 0-Cu and (b) 1-Cu steel.

3.6 Microscopic characterization

To reveal the relationship among the chemical composition, temperature, and deformation mechanisms, the microstructure of the two steels after deforming to different strains at 293 and 77 K were characterized with TEM. Fig. 10a and 10b show the typical bright-field TEM micrograph of the 0-Cu steel deformed to a true strain of ~0.3 at 293 K. The corresponding selected area diffraction pattern (SAED) was inserted in Fig. 10a. After deformation, high density of dislocations and closely packed structures, which were identified as nano-sized primary twins accompanied with thin HCP plates (identified with SAED), were produced (Fig. 10a and 10b). The HRTEM image in Fig. 10c revealed that the twins and HCP plates were closely located and accompanied with active formation of stacking faults. These well-defined twins and HCP clusters penetrated the grain interior and subgrains, leading to the continuous segmentation of grains. The mean free path of dislocations was reduced effectively and high density of dislocations (Fig. 10b) were trapped among them, thus providing significant strain hardening effects (so-called "dynamic Hall-Petch effect") [4].

As shown in Fig. 10d, the introduction of new interfaces (i.e., TBs) and similar dislocation-twin interaction were also observed in the deformed 1-Cu steel at 293 K (Fig. 10d). The twinning activity of the 1-Cu steel is more active than that of 0-Cu steel as both primary and secondary twin system were observed (Fig. 10e). The two intersecting twin systems introduced a higher density of TBs, forming a hierarchical twin substructure. The structure of the hierarchical twin system was further revealed via HRTEM in Fig. 10f. The primary

twins were typically arranged in the form of parallel bundles and their boundaries consist of stacking faults. The secondary twins formed from closely packed stacking faults intersecting with the primary twin. Apart from the crossing twinning networks, the active formation and following reaction of stacking faults, e.g., Lomer-Cottrell (L-C) locks, were also observed during the plastic straining.

The formation of twins, martensitic phase transformation, and L-C locks are closely related to the activity of stacking faults. Due to the low SFE of the steel, the dissociation of perfect dislocations can easily occur on two 60° inter-crossing crystallographic planes of (111) and $(11\bar{1})$, where numerous closely-packed stacking faults can be observed [40]. Twins can be formed by the glide of $\frac{a}{6}\langle 11\bar{2}\rangle$-type Shockley partial dislocations on consecutive (111) planes of the FCC matrix. When partial dislocation glide on every second (111) plane, the parent FCC phases with stacking sequence of …ABCABC… will transfer into HCP phases with …ACACAC… stacking sequence. Continuously produced partial dislocations on surrounding (111) planes can thicken the twins or HCP plates. Meanwhile, after the dissociation of perfect dislocations, the reaction of two leading partial dislocations from different slip systems can further lead to a high formation probability of a stair-rod dislocation via [41]:

$$\frac{a}{6}\langle 2\bar{1}\bar{1}\rangle + \frac{a}{6}\langle \bar{1}21\rangle \rightarrow \frac{a}{6}\langle 110\rangle \tag{14}$$

, the Burgers vector of stair-rod dislocation is perpendicular to the dislocation line and does not locate at the two {111} planes, making them sessile and hard to glide. These stair-rod dislocations are known as Lomer-Cottrell locks (marked with arrows in Fig. 10f) [42]. It is indicated that L-C locks play an important role in the strain hardening of FCC alloys [43]. The L-C locks show a high capability of accumulating dislocations as four dislocation segments can be pinned by each L-C lock. As the L-C locks are usually very short in length and can equivalently act as pinning points, the strengthening effects of L-C locks are very similar to Orowan's strengthening based on the orientation-dependent line tension model [44]. Meanwhile, the L-C locks can also become unlocked after interacting with traveling dislocations driven by external stress [45].

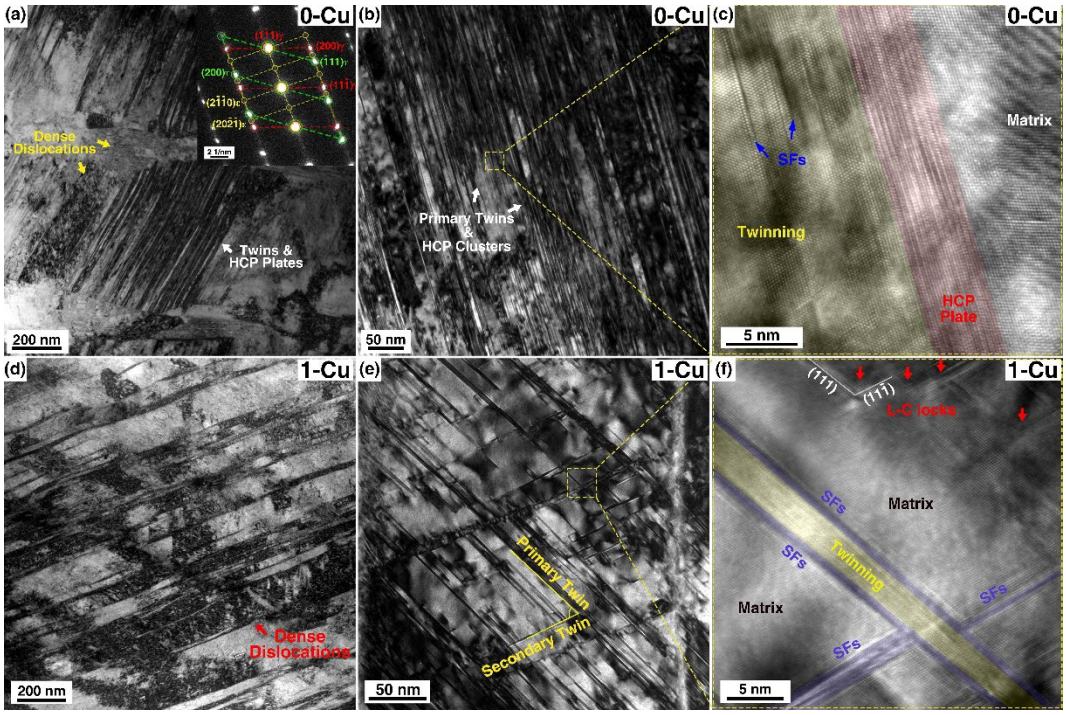

Fig. 10 Microstructure of the 0-Cu and 1-Cu steel deformed to true strain of ~0.3 at 293 K: (a) typical bright-field TEM image and corresponding selected area diffraction (SAED) pattern, 0-Cu; (b) higher magnification of (a); (c) HRTEM image of the rectangle area in (b); (d) typical bright-field image, 1-Cu; (e) higher magnification of (d); (f) HRTEM image of the rectangle area in (e).

The microstructure of the two steels deformed to similar strain levels of ~0.15 and ~0.3 at 77 K was compared in Fig. 11. Fig. 11a and 11b show the high density of mechanical twins formed in the 0-Cu and 1-Cu steels deformed to a true strain of ~0.15, respectively. Fig. 11c presents the HAADF image of the 0-Cu steel at a true strain of ~0.3, showing that the parent FCC matrix were transferred HCP plates. The HCP plates can be identified with the SAED pattern inserted in Fig. 11e, where HCP plates were entangled with dense dislocations. The martensite transformation can be ascribed to the lowered SFE caused by temperature decreasing, motivating the overlapping of the stacking faults on every other {111} plane [46]. The microstructure of the newborn HCP plates (the yellow square area in Fig. 11e) was revealed by HRTEM in Fig. 11g. It shows that the HCP phase exist in the form of parallel thin plates, separated by one or two stacking faults. This indicates that with the decrease of temperature (from 293 to 77 K) and SFE (from 26.8±0.5 to 15.5±1.7 mJm^{-2}), the martensite phase transformation gradually became the main deformation mechanism

of the 0-Cu steel. This result is in good accordance with the neutron diffraction results in Fig. 4 and SFE-deformation mechanism map in Fig. 8.

The deformation microstructure of the 1-Cu steel (at a true strain of ~0.3, 77 K) was revealed with HAADF image in Fig. 11d and bright-field TEM image in Fig. 11f. As the deformation temperature decreased to 77 K, the density of the hierarchy twin structure increased significantly compared to that at 293 K (Fig. 10). The abundance of primary and secondary twins introduced a much higher density of interfaces than that at 293 K, leading to more significant segmentation of the grains into ultrafine microstructural entities. The square frame area in Fig. 11f was further analyzed with HRTEM in Fig. 11h. It is a nanotwin-HCP structure consisting of two parallel twins with thin HCP plates located at their boundaries. The TBs can serve as preferable nucleation sites for HCP plates [47]. The extended dissociated dislocations can react with coherent TBs: the leading partial dislocation can decompose into a stair-rod partial and a glissile partial along the boundaries, forming a favorable site for the HCP formation [47]. The HCP phase has a very narrow width (~2 nm) and a low volume fraction at ~0.3 true strain, which may explain that only a very weak diffraction peak of ε-$\left(10\bar{1}1\right)$ was detected in the neutron diffraction spectra (Fig. 4). Besides, a high density of stacking faults was also observed among the FCC matrix. This indicates that twinning is still the main deformation mechanism of the 1-Cu steel at 77 K as only a very trace amount of HCP phases can be identified. The decrease of deformation temperature from 293 to 77 K largely promoted the formation of (primary and secondary) twins, thus providing a higher strain hardening effect.

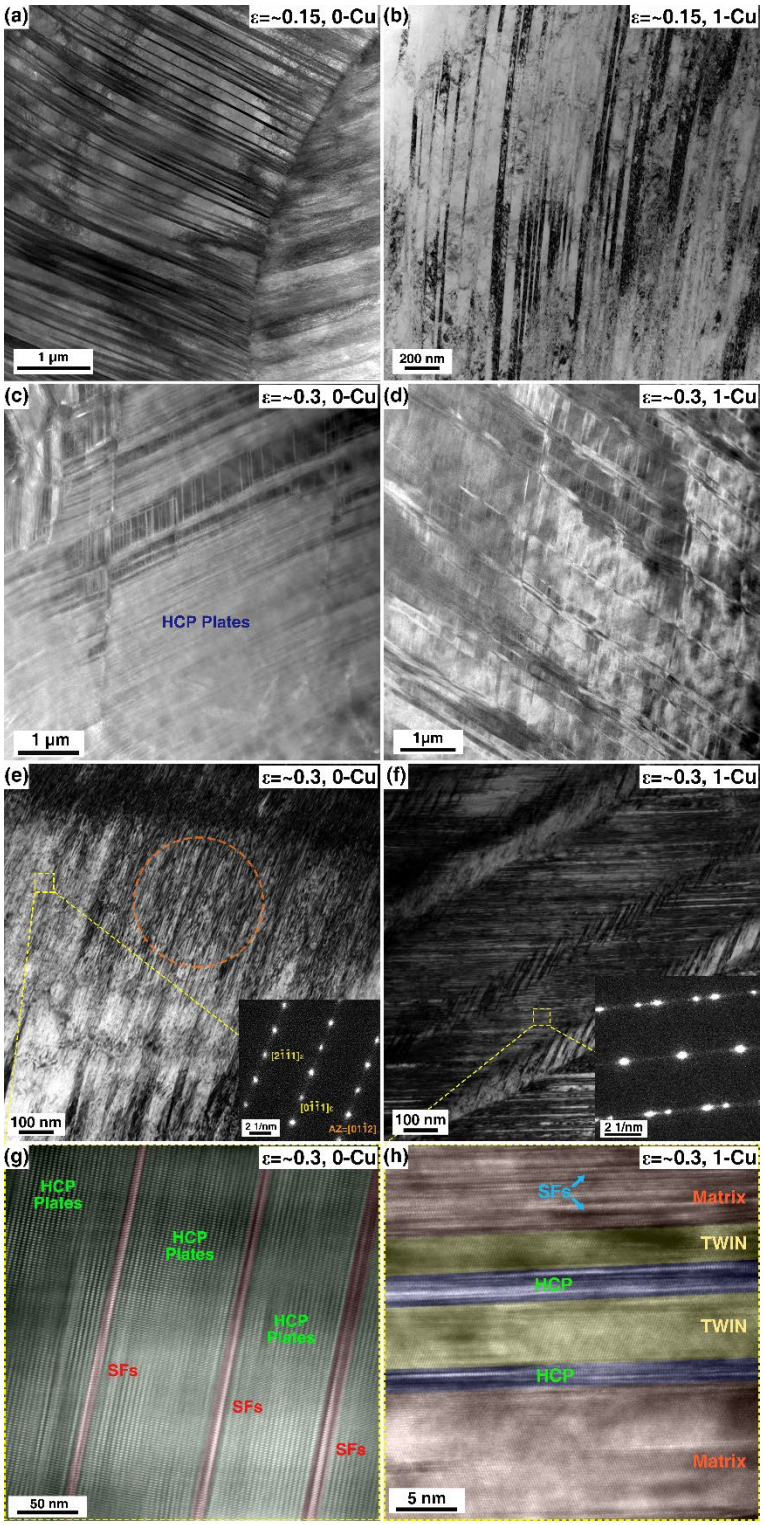

Fig. 11 The microstructure of the 0-Cu and 1-Cu steel deformed to different strain levels at 77 K: (a) and (b) typical bright-field TEM image of the 0-Cu and 1-Cu steel with a strain of ~0.15, respectively; (c) and (d) HAADF image of the 0-Cu and 1-Cu steel with a strain of ~0.3, respectively; (e) bright-field image of the 0-Cu and 1-Cu steel with a strain of ~0.3, respectively; (g) HRTEM image of the yellow square area in (e); (h) HRTEM image of the yellow square area in (f).

Therefore, the deformation behaviors of the two steels at 77 K can be summarized and schematically illustrated in Fig. 12. Originally, both steels showed low dislocation density and a high fraction of annealing twins distributed within the grain interiors. For the 0-Cu steel, dislocation multiplication/gliding, the primary twinning, and slight phase transformation dominated the strain hardening behavior at low strain levels. This originates from its low SFE locates very close to the twinning/phase transformation boundary (Fig. 8). The low SFE can decrease the critical stress for activating TWIP and TRIP effects [48]. While at high strains, in addition to the continuous increase of dislocation density, the formation and following growth of twins and HCP plates became the main deformation mechanisms, playing an important role in withstanding external stress and providing larger ductility. For the 1-Cu steel, it produced a high density of twins, stacking faults, dislocations, and L-C locks at low strains. The following deformation promoted the formation and growth of primary/secondary twins, forming three-dimensional hierarchical twinning systems and trapping dense dislocations in the intra-twin zones.

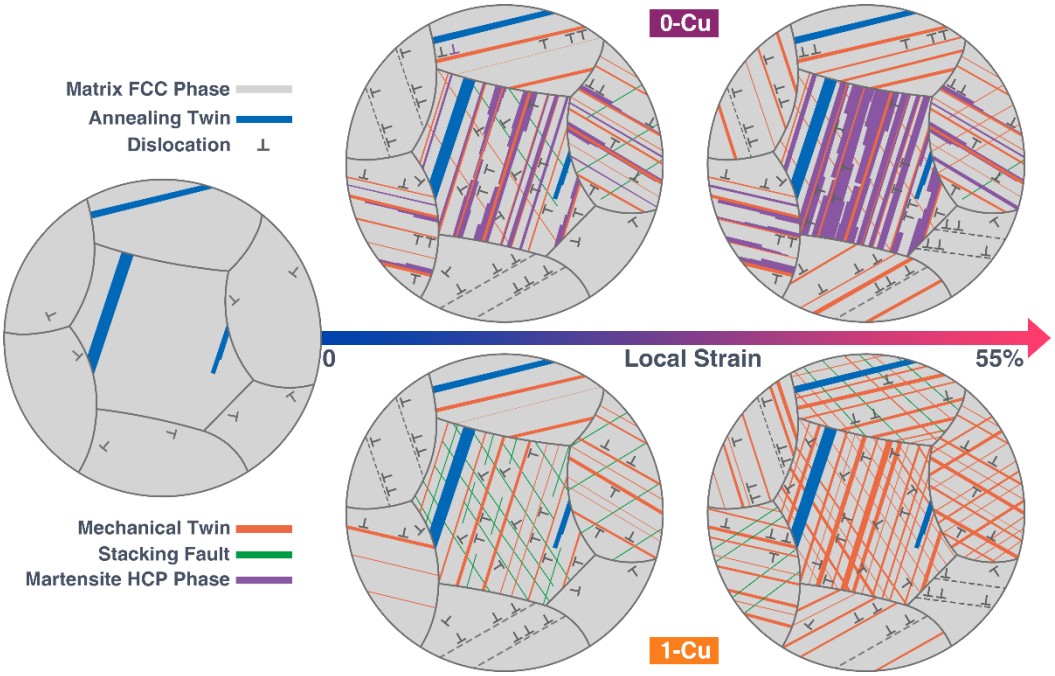

Fig. 12 Schematic sketches illustrating the sequence of micro-processes in the 0-Cu and 1-Cu steel during deforming at 77 K.

4. Discussion

The neutron diffraction and post-mortem TEM characterization indicate that the deformation behavior of the 0-Cu steel is a mixture of dislocation multiplication, twinning (at low strain levels), and phase transformation (at high strain levels). But for the 1-Cu steel, which has an overall higher SFE than the 0-Cu steel, dislocation motion and twinning are the dominant deformation mechanism during the whole plastic stage. Therefore, the total flow stress (σ_{flow}) of the two TWIP steels should combine the contributions of the yield stress (σ_y) and an incremental strain hardening effects (σ_{sh}) during plastic deformation [49]:

$$\sigma_{flow} = \sigma_y + \sigma_{sh} \tag{15}$$

First, we address the first term on the right, σ_y. According to Ref. [49], the yield stress is a combination of various strengthening effects:

$$\sigma_y = \sigma_{fr} + \sigma_p + \sigma_{dis}^0 + \sigma_{gb} \tag{16}$$

, where σ_{fr} is the lattice friction stress, i.e., intrinsic lattice resistance and the solid solution strengthening effects, σ_p represents the precipitation hardening, σ_{dis}^0 is the forest hardening effects due to the initial dislocation density of the virgin samples, σ_{gb} is the grain boundary hardening. For the two steels used in the present study, the σ_p can be eliminated since no precipitates were observed, at least from the neutron diffraction spectra (Fig. 4) and TEM observation (Fig. 10 and Fig. 11). According to Ref. [50], the forest strengthening effect of dislocations can be calculated with the Taylor equation:

$$\sigma_{dis} = M\alpha Gb\rho^{1/2}, \tag{17}$$

where M=3.06 is the Taylor factor, α=0.26 is a constant for scaling the interaction strength between dislocations [51,52]. According to the neutron diffraction results, the dislocation density of the two as-fabricated steels was about 7×10^{13} m^{-2}, contributing ~106 MPa to the YS. The hardening effects of grain boundaries can be well described with the Hall-Petch equation [53]:

$$\sigma_{GB} = \sqrt{\frac{G(T)}{G(RT)}} K_{gb} d^{-1/2}, \tag{18}$$

where the Hall-Petch coefficient (K_{gb}) of 0.357 MPa·m$^{0.5}$ was used according to Refs. [4,54], *G(T)* and *G(RT)* are the shear modulus at a given temperature and room temperature, respectively. Based on the average grain size of 14.5 ± 1.3 μm, the grain boundaries contributed ~95 MPa to the yield stress. Therefore, the lattice friction stress of the two steels can be calculated with Eq. (16). As shown in Fig. 13a, with the decrease of deformation temperature, the lattice friction stress of the two steels can increase almost linearly with very similar slopes (1.651 MPa·K^{-1} for 0-Cu steel and 1.717 MPa·K^{-1} for 1-Cu steel). It is worth noting that the 1-Cu steel shows overall higher (~90 MPa) lattice friction stress than the 0-Cu steel at all three temperatures. This can be ascribed to the stronger solid solution strengthening effects brought from Cu addition [18,20,55].

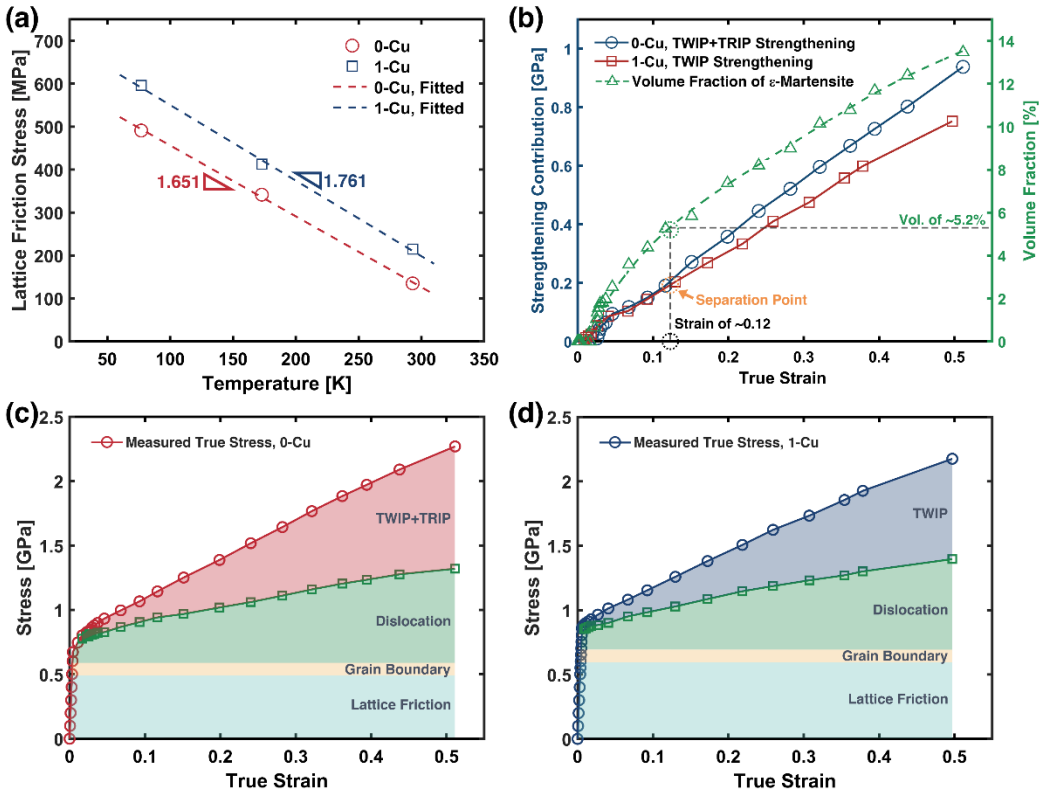

Fig. 13 Strengthening effects analysis of the 0-Cu and 1-Cu steel during deforming at 77 K: (a) the lattice friction stress evolution plotted as a function of temperature; (b) the evolution of strengthening contribution of TWIP of the 1-Cu steel and TWIP+TRIP of the 0-Cu steel with respect to true strain; (c) and (d) the respective contribution of multiple strengthening mechanisms to the total flow stress of the 0-Cu and 1-Cu steel, respectively.

Next, we address the strengthening effects during plastic deformation. According to Refs. [4,49], several strengthening effects including (1) dislocation multiplication, (2) twinning, and (3) martensite phase transformation (σ_{tr}) can collaboratively contribute to the incremental stress at the plastic stage:

$$\sigma_{sh} = \sigma_{dis}^{p} + \sigma_{tw} + \sigma_{tr} \tag{19}$$

, where σ_{dis}^{p} is the strengthening contribution from the dislocations produced during straining. Combining Eq. (15), (16), and (19), the contribution from twinning (σ_{tw}) and/or phase transformation (σ_{tr}) can be calculated with:

$$\sigma_{tw} + \sigma_{tr} = \sigma - \sigma_{gb} - \sigma_{fr} - \sigma_{dis}. \tag{20}$$

For the 1-Cu steel, a trace amount of the transformed ε-martensite phase has been identified (not detectable via neutron diffraction) and preferably exists with a very wide spacing distance and thin thickness (<5 nm) (Fig. 5 and Fig. 12f). These stand-alone HCP plates have a very limited ability to impede dislocation motions and produce strengthening effects [4]. The contribution from martensite phase transformation is thus neglected for the 1-Cu steel. However, when deforming the 0-Cu steel at 77 K, strain-induced hard HCP plates serve as an additional strengthening source, which can introduce extra FCC/HCP interfaces with high-stress concentration and reduce the mean free path of dislocation motions [56]. Therefore, a synergistic strengthening effect of TWIP and TRIP was considered in deforming the 0-Cu steel at 77 K. The evolution of volume fraction of HCP phases of the 0-Cu steel and strengthening contribution of the TWIP effect (for the 1-Cu steel) and TWIP+TRIP effect (for the 0-Cu steel) at 77 K were plotted as a function of true strain in Fig. 13b. Starting from a very low level (~50 MPa), the two curves increased linearly with true strain and were almost overlapped before strain reaching 0.12 and the volume fraction of HCP martensite reaching ~5.2% (separation point). This indicates the strengthening effects of HCP plates is negligible with a limited volume fraction (lower than 5.2%), where most of them were distributed distantly or along with TBs. The two curves then gradually separated, and the difference became wider with the increase of strain. At the true strain of

~0.5, extensive TBs contributed ~810 MPa in 1-Cu steel, while the twin and HCP-martensite/austenite interfaces in 0-Cu steel provided ~940 MPa to the total flow stress. This indicates that the abundance of HCP phases in the 0-Cu steel can provide more significant strain hardening effects than hierarchy twin networks produced in the 1-Cu steel. The strengthening contribution from different resources were plotted with the true stress-strain curves in Fig. 13c (0-Cu) and 13d (1-Cu).

According to our SHR results in Fig. 2, both twinning and martensite phase transformation can provide steady and significant strengthening effects and improve the ductility of the steels. But they may influence the mechanical performance differently. On one hand, the abundance of strain-induced TBs can provide continuous strain hardening effects by penetrating the grain interior, forming dense three-dimensional networks, and subdividing the grains into nano-scaled substructures. The dislocation-twin, dislocation-dislocation, and twin-twin interactions were significantly promoted, thus offering substantial work-hardening effects. Due to the segmentation of the grains, the strengthening effects of TBs are generally considered analogous to grain boundaries. The twin spacing dependent strengthening effect is thus represented similar to the classical Hall-Petch relation [57]:

$$\sigma_{tw} = k_{TB} / \sqrt{t}, \tag{21}$$

where t is the average twin spacing and k_{TB} is a constant. Meanwhile, due to the inhabitation of TBs to dislocations, high-density orderly arranged interfacial dislocation can be observed along with TBs. The dynamic recovery of dislocations can be effectively reduced by dense hierarchical twin networks [58]. This may explain the higher dislocation density when deforming at lower temperatures (Fig. 9).

On the other hand, twinning can also improve the plasticity of the 1-Cu steel. TBs can be penetrated by dislocations with decreasing the twin lamella thickness and higher external stress [57], allowing further dislocation motion and providing larger plasticity. For the present study, the strain-induced TBs, especially the secondary twins, has a very narrow width (less than ~5 nm, Fig. 10 and 11), which may relieve the stress concentration along with TBs and reduce the strain hardening effect. Furthermore, the softening effect of twinning originates from its role as an effective and supportive deformation mechanism.

TBs can serve as adequate pathways for easy glide and cross-slip of dislocations, enabling the alloy to accommodate extensive plastic deformation at high strain levels and postpone necking [59].

Similarly, the transformation from FCC to HCP plates is expected to produce a significant strengthening effect. The strengthening effects of strain-induced HCP plates are based on continuous segregating grains by introducing extra phase-matrix interfaces, where dislocations pile up can be significantly promoted after active dislocation motions. This can create significant back stresses, which are capable of reducing the mobility of dislocations, dynamic recovery, and thus improving work hardening rate [60]. Unlike the thin twins, the HCP plates serve as stronger dislocation barriers due to either <c> or <c+a> dislocations are needed for passing edge dislocations into the HCP phase, and the critical resolved shear stress of motivating these dislocations are very high [61]. More importantly, the HCP plates can also create very strong barriers for twinning on impinging slip systems, and motivating intragranular rotations [47]. On the other hand, the high density of HCP plates also deteriorate the ductility of the 0-Cu steel due to the stress concentration at HCP/TB or HCP/FCC interfaces is too high and induce the quasi-cleavage fracture [22].

The strengthening effects of dislocation and faulted structures (TWIP and TRIP) were plotted as a function of true strain in Fig. 14a and b, respectively. When deforming the 0-Cu steel to a true strain of ~0.5, the strengthening contribution from dislocation (σ_{dis}) increased from ~493 MPa at 293 K to ~690 MPa at 77 K. Meanwhile, the contribution from the faulted structures (σ_{fs}) was ~780 MPa at 293 K (from TWIP), which increased to ~940 MPa at 77 K (from TWIP and TRIP). While the strengthening effect is less significant in the 1-Cu steel at a similar strain level: σ_{dis} was ~470 MPa at 293 K and ~770 MPa at 77 K while σ_{fs} was ~640 MPa at 293 K and 810 MPa at 77 K. The hardening effects showed an almost linear increase with true strain. After linear fitting, their slopes were defined as the dislocation-induced ($\partial\sigma_{dis}/\partial\varepsilon$) and faulted structures-induced ($\partial\sigma_{fs}/\partial\varepsilon$) hardening rates, respectively. This indicates that the high strengthening effects can be ascribed to concurrent strengthening effects from dislocation, TWIP, and TRIP, which can be enhanced with the decrease of deformation temperature and SFE. The

influence of temperature on the hardening rates of the three steels, the 0-Cu, 0.5-Cu [4], and 1-Cu steel, was also illustrated in Fig. 14c. This indicates that both $\partial\sigma_{dis}/\partial\varepsilon$ and $\partial\sigma_{fs}/\partial\varepsilon$ increased almost linearly with temperature decreasing. Their relationship can thus be described as:

$$-m_{dis} = \frac{\partial\sigma_{dis}}{\partial\varepsilon\partial T} \tag{22}$$

$$-m_{fs} = \frac{\partial\sigma_{fs}}{\partial\varepsilon\partial T} \tag{23}$$

, where the m_{dis} and m_{fs} are the slopes of the hardening rate-temperature curves of the dislocation and faulted structures, respectively. After linear fitting, m_{dis} of the three high Mn steels maintained at a very similar level of ~2.0 MPa·K^{-1}. The 1-Cu and 0.5-Cu steels have m_{fs} = ~1.1 MPa·K^{-1}, lower than that of the 0-Cu steel, m_{fs} = 1.89 MPa·K^{-1}. This is due to the synergistic hardening effects of TWIP and TRIP of the 0-Cu steel at 77 K.

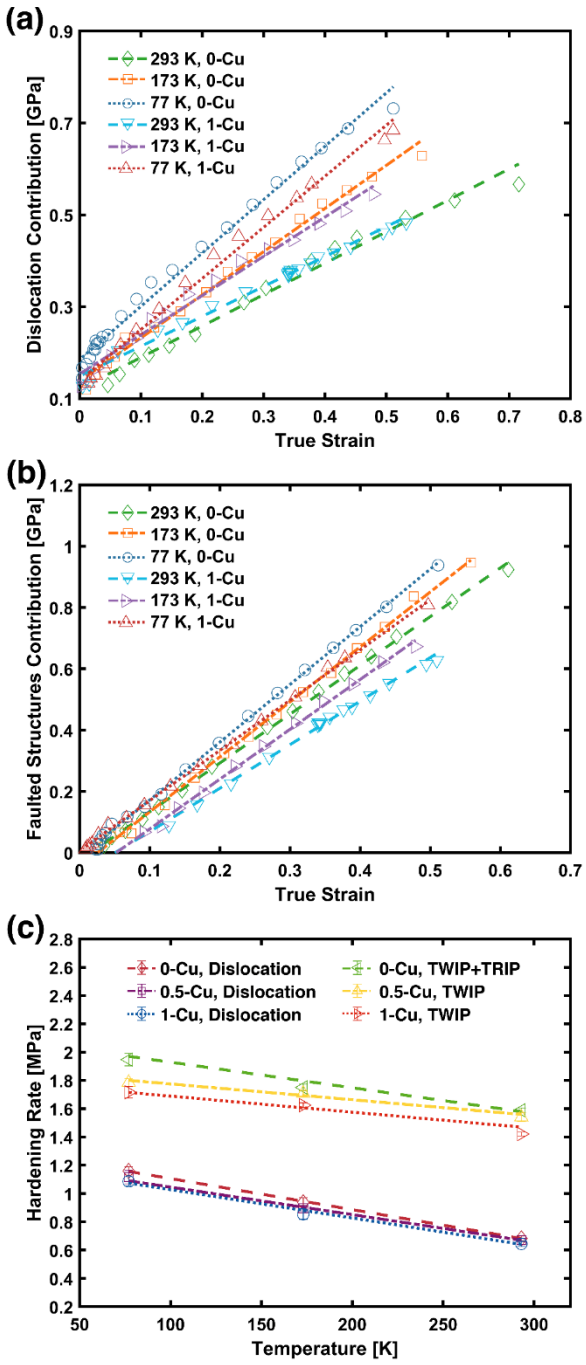

Fig. 14 Strengthening hardening effect of (a) dislocations and (b) TWIP and TRIP; (c) temperature dependence of the hardening rate from dislocations and faulted structures.

5. Conclusions

The role of Cu alloying and deformation temperature in tailoring stacking fault energy, deformation mechanisms, and mechanical performance of two high Mn steels at the low-temperature range (from 293 to 77 K) were investigated with *in situ* neutron diffraction tensile tests and correlated post-mortem microscopic characterization. The investigation leads to the following conclusions:

(1) The tensile strength increased steadily with temperature decreasing. At 293 K, the YS and UTS of the 0-Cu steel are 336 MPa and 930 MPa, respectively, while the 1-Cu steel showed a higher YS of 429 MPa but lower UTS of 876 MPa. At 77 K, the 0-Cu steel showed a high YS of 700 MPa and UTS of 1358 MPa while the corresponding data of the 1-Cu steel can reach 793 MPa and 1323 MPa. Meanwhile, the large elongation was maintained even at 77 K with uniform elongation of ~0.68 and ~0.64 for the 0-Cu and 1-Cu steel, respectively.

(2) Cu alloying serves as an effectively method in tailoring SFE and deformation mechanisms at low temperatures. The stacking fault energy of the two steels was determined with both thermodynamical modeling and neutron diffraction measurements. The results show that the SFE increased with Cu addition and decreased linearly with the drop of temperature (with a slope of ~0.06 $mJm^{-2}K^{-1}$). The SFE of the 0-Cu steel decreased from 26.8±0.5 mJm^{-2} at 293 K to 15.5±1.7 mJm^{-2} at 77 K. The dominant deformation mechanism of the 0-Cu steel switched from twinning (at 293 and 173 K) to martensite phase transformation (at 77 K). The 1wt.% Cu addition enhanced the SFE with ~5 mJm^{-2}, making twinning the main deformation mechanism for the 1-Cu steel.

(3) The lattice friction stress was increased by decreasing temperature and Cu alloying. The 1wt.% of Cu addition can enhance ~82 MPa of the lattice friction stress. Starting from 135 MPa (0-Cu) and 215 MPa (1-Cu), the lattice friction stress increased linearly with the temperature dropping with a slope of 1.651 $MPa \cdot K^{-1}$ for the 0-Cu steel and 1.761 $MPa \cdot K^{-1}$ for the 1-Cu steel.

(4) The dislocation density of the two steels was calculated with the modified Williamson-Hall method. The dislocation density was at around 7×10^{13} m^{-2} before deformation. The

dislocation density increased almost linearly with strain after yielding. Its increase rate was higher at lower deformation temperatures. The deformed 0-Cu steel showed a higher level of dislocation density than the 1-Cu alloy. When deforming at 77 K to a true strain of ~0.5, the highest dislocation density of both steels was achieved (~2.5×10^{15} m^{-2} for the 0-Cu steel and ~2.0×10^{15} m^{-2} for the 1-Cu steel).

(5) The strengthening effects of both dislocation and faulted structures (twins and martensite) are significant and increase as the temperature/SFE decreased. For the 0-Cu steel deformed to a true strain of ~0.5, dislocation contributed ~470 MPa at 293 K and ~730 MPa at 77 K, while the faulted structures contributed ~770 MPa at 293 K from TWIP only, which increased to ~940 MPa at 77 K from both TWIP and TRIP effects.

CRediT authorship contribution statement

L. Tang: Data curation, Formal analysis, Visualization, Writing – original draft, Writing - Review & Editing. **F.Q. Jiang**: Investigation, Writing - Review & Editing. **S. Kabra**: Investigation, Writing – review & editing. **H.B. Liu**: Investigation, Writing – review & editing. **B. Cai**: Supervision, Conceptualization, Methodology, Formal analysis, Writing-Reviewing & Editing.

Acknowledgments

The authors thank the ISIS neutron and muon source (the Rutherford Appleton Laboratory, UK) for providing the beamtime (RB1810732, and RB1920111, and RB2010324) and staff at ENGIN-X beamline for support.

References

[1] Y.F. Shen, N. Jia, R.D.K. Misra, L. Zuo, Softening behavior by excessive twinning and adiabatic heating at high strain rate in a Fe-20Mn-0.6C TWIP steel, Acta Mater. 103 (2016) 229–242. https://doi.org/10.1016/j.actamat.2015.09.061.

[2] C. Zheng, Q. Zhen, Y. Wang, N. Li, Low temperature macro- and micro-mechanical behavior of an ultrafine-grained metastable 304 austenitic stainless steel investigated by in situ high-energy X-ray diffraction, Mater. Sci. Eng. A. 817 (2021) 141295. https://doi.org/10.1016/j.msea.2021.141295.

[3] S. Hany, M. Milochova, K. Littrell, R. Lorange, J.-B. Vogt, E. Abi-Aad, E. Bychkov,

Advanced characterization of cryogenic 9Ni steel using synchrotron radiation, neutron scattering and 57Fe Mössbauer spectroscopy, Mater. Des. 146 (2018) 219–227. https://doi.org/10.1016/j.matdes.2018.03.024.

[4] L. Tang, L. Wang, M. Wang, H. Liu, S. Kabra, Y. Chiu, B. Cai, Synergistic deformation pathways in a TWIP steel at cryogenic temperatures: In situ neutron diffraction, Acta Mater. 200 (2020) 943–958. https://doi.org/10.1016/j.actamat.2020.09.075.

[5] S. Curtze, V.-T.T. Kuokkala, Dependence of tensile deformation behavior of TWIP steels on stacking fault energy, temperature and strain rate, Acta Mater. 58 (2010) 5129–5141. https://doi.org/10.1016/j.actamat.2010.05.049.

[6] O.A. Zambrano, Stacking Fault Energy Maps of Fe–Mn–Al–C–Si Steels: Effect of Temperature, Grain Size, and Variations in Compositions, J. Eng. Mater. Technol. 138 (2016) 041010. https://doi.org/10.1115/1.4033632.

[7] Y. Wang, M. Zhang, Q. Cen, W. Wang, X. Sun, A novel process combining thermal deformation and intercritical annealing to enhance mechanical properties and avoid Lüders strain of Fe-0.2C–7Mn TRIP steel, Mater. Sci. Eng. A. 839 (2022) 142849. https://doi.org/10.1016/J.MSEA.2022.142849.

[8] Y.F. Shen, Y.D. Wang, X.P. Liu, X. Sun, R. Lin Peng, S.Y. Zhang, L. Zuo, P.K. Liaw, Deformation mechanisms of a 20Mn TWIP steel investigated by in situ neutron diffraction and TEM, Acta Mater. 61 (2013) 6093–6106. https://doi.org/10.1016/J.ACTAMAT.2013.06.051.

[9] S. Allain, J.P. Chateau, O. Bouaziz, S. Migot, N. Guelton, Correlations between the calculated stacking fault energy and the plasticity mechanisms in Fe-Mn-C alloys, Mater. Sci. Eng. A. 387–389 (2004) 158–162. https://doi.org/10.1016/j.msea.2004.01.059.

[10] A. Dumay, J.-P.P. Chateau, S. Allain, S. Migot, O. Bouaziz, Influence of addition elements on the stacking-fault energy and mechanical properties of an austenitic Fe-Mn-C steel, Mater. Sci. Eng. A. 483–484 (2008) 184–187. https://doi.org/10.1016/j.msea.2006.12.170.

[11] L. Tang, K. Yan, B. Cai, Y. Wang, B. Liu, S. Kabra, M.M. Attallah, Y. Liu, Deformation mechanisms of FeCoCrNiMo0.2 high entropy alloy at 77 and 15 K, Scr. Mater. 178 (2020) 166–170. https://doi.org/10.1016/j.scriptamat.2019.11.026.

[12] J.K. Kim, B.C. De Cooman, Stacking fault energy and deformation mechanisms in Fe-xMn-0.6C-yAl TWIP steel, Mater. Sci. Eng. A. 676 (2016) 216–231. https://doi.org/10.1016/J.MSEA.2016.08.106.

[13] A. Saeed-Akbari, A. Schwedt, W. Bleck, Low stacking fault energy steels in the context of manganese-rich iron-based alloys, Scr. Mater. 66 (2012) 1024–1029. https://doi.org/10.1016/j.scriptamat.2011.12.041.

[14] X.D. Wang, B.X. Huang, Y.H. Rong, L. Wang, Microstructures and stability of retained austenite in TRIP steels, Mater. Sci. Eng. A. 438–440 (2006) 300–305. https://doi.org/10.1016/J.MSEA.2006.02.149.

[15] B. Cai, B. Liu, S. Kabra, Y. Wang, K. Yan, P.D. Lee, Y. Liu, Deformation mechanisms of Mo alloyed FeCoCrNi high entropy alloy: In situ neutron diffraction, Acta Mater. 127 (2017) 471–480. https://doi.org/10.1016/j.actamat.2017.01.034.

[16] X. Rao, Y. Wu, X. Pei, Y. Jing, L. Luo, Y. Liu, J. Lu, Influence of rolling temperature on microstructural evolution and mechanical behavior of AZ31 alloy with accumulative roll bonding, Mater. Sci. Eng. A. 754 (2019) 112–120. https://doi.org/10.1016/j.msea.2019.03.047.

[17] S. Lee, J. Kim, S.J. Lee, B.C. De Cooman, Effect of Cu addition on the mechanical behavior of austenitic twinning-induced plasticity steel, Scr. Mater. 65 (2011) 1073–1076. https://doi.org/10.1016/J.SCRIPTAMAT.2011.09.019.

[18] X. Peng, D. Zhu, Z. Hu, W. Yi, H. Liu, M. Wang, Stacking fault energy and tensile deformation behavior of high-carbon twinning-induced plasticity steels: Effect of Cu addition, Mater. Des. 45 (2013) 518–523. https://doi.org/10.1016/J.MATDES.2012.09.014.

[19] S.J. Kim, C.G. Lee, T.H. Lee, C.S. Oh, Effect of Cu, Cr and Ni on mechanical properties of 0.15 wt.% C TRIP-aided cold rolled steels, Scr. Mater. 48 (2003) 539–544. https://doi.org/10.1016/S1359-6462(02)00477-3.

[20] B. Kim, S.G. Lee, D.W. Kim, Y.H. Jo, J. Bae, S.S. Sohn, S. Lee, Effects of Ni and Cu addition on cryogenic-temperature tensile and Charpy impact properties in austenitic 22Mn-0.45C–1Al steels, J. Alloys Compd. 815 (2020) 152407. https://doi.org/10.1016/J.JALLCOM.2019.152407.

[21] B.M. Gonzalez, C.S.B. Castro, V.T.L. Buono, J.M.C. Vilela, M.S. Andrade, J.M.D. Moraes, M.J. Mantel, The influence of copper addition on the formability of AISI 304 stainless steel, Mater. Sci. Eng. A. 343 (2003) 51–56. https://doi.org/10.1016/S0921-5093(02)00362-3.

[22] J.H. Choi, M.C. Jo, H. Lee, A. Zargaran, T. Song, S.S. Sohn, N.J. Kim, S. Lee, Cu addition effects on TRIP to TWIP transition and tensile property improvement of ultra-high-strength austenitic high-Mn steels, Acta Mater. 166 (2019) 246–260. https://doi.org/10.1016/j.actamat.2018.12.044.

[23] G.B. Olson, M. Cohen, A general mechanism of martensitic nucleation: Part I. General concepts and the FCC → HCP transformation, Metall. Trans. A. 7 (1976) 1897–1904. https://doi.org/10.1007/BF02659822.

[24] Y.K. Lee, C.S. Choi, Driving force for γ → ε martensitic transformation and stacking fault energy of γ in Fe-Mn binary system, Metall. Mater. Trans. A Phys. Metall. Mater. Sci. 31 (2000) 355–360. https://doi.org/10.1007/s11661-000-0271-3.

[25] P.H. Adler, G.B. Olson, W.S. Owen, Strain Hardening of Hadfield Manganese Steel, Metall. Mater. Trans. A. 17 (1986) 1725–1737. https://doi.org/10.1007/BF02817271.

[26] G.L. Huang, D.K. Matlock, G. Krauss, Martensite formation, strain rate sensitivity, and deformation behavior of type 304 stainless steel sheet, Metall. Trans. A, Phys. Metall. Mater. Sci. 20 A (1989) 1239–1246. https://doi.org/10.1007/BF02647406.

[27] S. Curtze, V.-T. Kuokkala, A. Oikari, J. Talonen, H. Hänninen, Thermodynamic modeling of the stacking fault energy of austenitic steels, Acta Mater. 59 (2011) 1068–1076. https://doi.org/10.1016/j.actamat.2010.10.037.

[28] L. Li, T.Y. Hsu, X. Zuyao, GIBBS FREE ENERGY EVALUATION OF THE FCC(y) AND HCP(&) PHASES IN FE-MN-S1 ALLOYS, Pergamon Calphad. 21 (1997) 443–448.

[29] G. Inden, The role of magnetism in the calculation of phase diagrams, Phys. B+C. 103 (1981) 82–100. https://doi.org/10.1016/0378-4363(81)91004-4.

[30] K. Ishida, Direct estimation of stacking fault energy by thermodynamic analysis, Phys. Status Solidi. 36 (1976) 717–728. https://doi.org/10.1002/pssa.2210360233.

[31] W.S. Yang, C.M. Wan, The influence of aluminium content to the stacking fault energy in Fe-Mn-Al-C alloy system, J. Mater. Sci. 25 (1990) 1821–1823. https://doi.org/10.1007/BF01045392.

[32] I.A. Yakubtsov, A. Ariapour, D.D. Perovic, Effect of nitrogen on stacking fault energy of f.c.c. iron-based alloys, Acta Mater. 47 (1999) 1271–1279. https://doi.org/10.1016/S1359-6454(98)00419-4.

[33] L. Tang, F.Q. Jiang, J.S. Wróbel, B. Liu, S. Kabra, R.X. Duan, J.H. Luan, Z.B. Jiao, M.M. Attallah, D. Nguyen-Manh, B. Cai, In situ neutron diffraction unravels deformation mechanisms of a strong and ductile FeCrNi medium entropy alloy, J. Mater. Sci. Technol. 116 (2022) 103–120. https://doi.org/10.1016/j.jmst.2021.10.034.

[34] Z. Wang, A.D. Stoica, D. Ma, A.M. Beese, Diffraction and single-crystal elastic constants of Inconel 625 at room and elevated temperatures determined by neutron diffraction, Mater. Sci. Eng. A. 674 (2016). https://doi.org/http://dx.doi.org/10.1016/j.msea.2016.08.010.

[35] X. Sun, S. Lu, R. Xie, X. An, W. Li, T. Zhang, C. Liang, X. Ding, Y. Wang, H. Zhang, L. Vitos, Can experiment determine the stacking fault energy of metastable alloys?, Mater. Des. 199 (2021) 109396. https://doi.org/10.1016/J.MATDES.2020.109396.

[36] E. El-Danaf, S.R. Kalidindi, R.D. Doherty, Influence of grain size and stacking fault energy on deformation twinning in fcc metals, Metall. Mater. Trans. A. 30 (1999) 1223–1999. https://doi.org/10.1007/s11661-001-0109-7.

[37] T. Ungár, G. Tichy, The Effect of Dislocation Contrast on X-Ray Line Profiles in Untextured Polycrystals, Phys. Status Solidi. 171 (1999) 425–434. https://doi.org/10.1002/(SICI)1521-396X(199902)171:2<425::AID-PSSA425>3.0.CO;2-W.

[38] I.C. Jung, B.C. De Cooman, Temperature dependence of the flow stress of Fe-18Mn-0.6C-xAl twinning-induced plasticity steel, Acta Mater. 61 (2013) 6724–6735. https://doi.org/10.1016/j.actamat.2013.07.042.

[39] E.I. Galindo-Nava, P.E.J. Rivera-Díaz-del-Castillo, Modelling plastic deformation in BCC metals: Dynamic recovery and cell formation effects, Mater. Sci. Eng. A.

558 (2012) 641–648. https://doi.org/10.1016/J.MSEA.2012.08.068.

[40] J.P. Hirth, J. Lothe, T. Mura, Theory of dislocations, J. Appl. Mech. 50 (1983) 476.

[41] X. Gao, Y. Lu, J. Liu, J. Wang, T. Wang, Y. Zhao, Extraordinary ductility and strain hardening of Cr26Mn20Fe20Co20Ni14 TWIP high-entropy alloy by cooperative planar slipping and twinning, Materialia. 8 (2019) 100485. https://doi.org/10.1016/j.mtla.2019.100485.

[42] J. Yoo, K. Choi, A. Zargaran, N.J. Kim, Effect of stacking faults on the ductility of Fe-18Mn-1.5Al-0.6C twinning-induced plasticity steel at low temperatures, Scr. Mater. 137 (2017) 18–21. https://doi.org/10.1016/J.SCRIPTAMAT.2017.04.037.

[43] X.L. Wu, Y.T. Zhu, Y.G. Wei, Q. Wei, Strong Strain Hardening in Nanocrystalline Nickel, Phys. Rev. Lett. 103 (2009) 1–4. https://doi.org/10.1103/PhysRevLett.103.205504.

[44] L. Dupuy, M.C. Fivel, A study of dislocation junctions in FCC metals by an orientation dependent line tension model, Acta Mater. 50 (2002) 4873–4885. https://doi.org/10.1016/S1359-6454(02)00356-7.

[45] J.H. Lee, T.B. Holland, A.K. Mukherjee, X. Zhang, H. Wang, Direct observation of Lomer-Cottrell Locks during strain hardening in nanocrystalline nickel by in situ TEM, Sci. Rep. 3 (2013) 1–6. https://doi.org/10.1038/srep01061.

[46] J.W. Brooks, M.H. Loretto, R.E. Smallman, Direct observations of martensite nuclei in stainless steel, Acta Metall. 27 (1979) 1839–1847. https://doi.org/10.1016/0001-6160(79)90074-9.

[47] J. Miao, C.E. Slone, T.M. Smith, C. Niu, H. Bei, M. Ghazisaeidi, G.M. Pharr, M.J. Mills, The evolution of the deformation substructure in a Ni-Co-Cr equiatomic solid solution alloy, Acta Mater. 132 (2017) 35–48. https://doi.org/10.1016/j.actamat.2017.04.033.

[48] D.R. Steinmetz, T. Jäpel, B. Wietbrock, P. Eisenlohr, I. Gutierrez-Urrutia, A. Saeed-Akbari, T. Hickel, F. Roters, D. Raabe, Revealing the strain-hardening behavior of twinning-induced plasticity steels: Theory, simulations, experiments, Acta Mater. 61 (2013) 494–510. https://doi.org/10.1016/j.actamat.2012.09.064.

[49] Z. Wu, H. Bei, G.M. Pharr, E.P. George, Temperature dependence of the mechanical properties of equiatomic solid solution alloys with face-centered cubic crystal structures, Acta Mater. 81 (2014) 428–441. https://doi.org/10.1016/j.actamat.2014.08.026.

[50] O. Bouaziz, N. Guelton, Modelling of TWIP effect on work-hardening, Mater. Sci. Eng. A. 319–321 (2001) 246–249. https://doi.org/10.1016/S0921-5093(00)02019-0.

[51] Y.Z. Li, Z.Y. Liang, M.X. Huang, Strengthening contributions of dislocations and twins in warm-rolled TWIP steels, Int. J. Plast. 150 (2022) 103198. https://doi.org/10.1016/J.IJPLAS.2021.103198.

[52] S. Brinckmann, T. Siegmund, Y. Huang, A dislocation density based strain gradient model, Int. J. Plast. 22 (2006) 1784–1797.

https://doi.org/10.1016/J.IJPLAS.2006.01.005.

[53] G. Ghosh, G.B. Olson, The isotropic shear modulus of multicomponent Fe-base solid solutions, Acta Mater. 50 (2002) 2655–2675. https://doi.org/10.1016/S1359-6454(02)00096-4.

[54] F. de las Cuevas, M. Reis, A. Ferraiuolo, G. Pratolongo, L.P. Karjalainen, J. Alkorta, J. Gil Sevillano, Hall-Petch Relationship of a TWIP Steel, Key Eng. Mater. 423 (2010) 147–152. https://doi.org/10.4028/www.scientific.net/KEM.423.147.

[55] Z.B. Jiao, J.H. Luan, Z.W. Zhang, M.K. Miller, W.B. Ma, C.T. Liu, Synergistic effects of Cu and Ni on nanoscale precipitation and mechanical properties of high-strength steels, Acta Mater. 61 (2013) 5996–6005. https://doi.org/10.1016/j.actamat.2013.06.040.

[56] B.C. De Cooman, Y. Estrin, S.K. Kim, Twinning-induced plasticity (TWIP) steels, Acta Mater. 142 (2018) 283–362. https://doi.org/10.1016/j.actamat.2017.06.046.

[57] P. Zhou, Z.Y. Liang, R.D. Liu, M.X. Huang, Evolution of dislocations and twins in a strong and ductile nanotwinned steel, Acta Mater. 111 (2016) 96–107. https://doi.org/10.1016/j.actamat.2016.03.057.

[58] C. Sun, D.W. Brown, B. Clausen, D.C. Foley, K.Y. Yu, Y. Chen, S.A. Maloy, K.T. Hartwig, H. Wang, X. Zhang, In situ neutron diffraction study on temperature dependent deformation mechanisms of ultrafine grained austenitic Fe–14Cr–16Ni alloy, Int. J. Plast. 53 (2014) 125–134. https://doi.org/10.1016/J.IJPLAS.2013.07.007.

[59] L. Zhu, H. Kou, J. Lu, On the role of hierarchical twins for achieving maximum yield strength in nanotwinned metals, Appl. Phys. Lett. 101 (2012) 081906. https://doi.org/10.1063/1.4747333.

[60] Y. Li, Y. Lu, W. Li, M. Khedr, H. Liu, X. Jin, Hierarchical microstructure design of a bimodal grained twinning-induced plasticity steel with excellent cryogenic mechanical properties, Acta Mater. 158 (2018) 79–94. https://doi.org/10.1016/j.actamat.2018.06.019.

[61] Y. Ma, F. Yuan, M. Yang, P. Jiang, E. Ma, X. Wu, Dynamic shear deformation of a CrCoNi medium-entropy alloy with heterogeneous grain structures, Acta Mater. 148 (2018) 407–418. https://doi.org/10.1016/j.actamat.2018.02.016.